

ARTICLE

FIT2 is an acyl-coenzyme A diphosphatase crucial for endoplasmic reticulum homeostasis

Michel Becuwe^{1,2,7}, Laura M. Bond^{1,2,7}, Antonio F.M. Pinto³, Sebastian Boland^{1,2,7} , Niklas Mejhert^{1,2,7}, Shane D. Elliott^{1,2,7,8}, Marcelo Cicconet⁴, Morven M. Graham⁵ , Xinran N. Liu⁵, Olga Ilkayeva⁶, Alan Saghatelian³ , Tobias C. Walther^{1,2,7,8*} , and Robert V. Farese Jr.^{1,2,7*} 

The endoplasmic reticulum is a cellular hub of lipid metabolism, coordinating lipid synthesis with continuous changes in metabolic flux. Maintaining ER lipid homeostasis despite these fluctuations is crucial to cell function and viability. Here, we identify a novel mechanism that is crucial for normal ER lipid metabolism and protects the ER from dysfunction. We identify the molecular function of the evolutionarily conserved ER protein FIT2 as a fatty acyl-coenzyme A (CoA) diphosphatase that hydrolyzes fatty acyl-CoA to yield acyl 4'-phosphopantetheine. This activity of FIT2, which is predicted to be active in the ER lumen, is required in yeast and mammalian cells for maintaining ER structure, protecting against ER stress, and enabling normal lipid storage in lipid droplets. Our findings thus solve the long-standing mystery of the molecular function of FIT2 and highlight the maintenance of optimal fatty acyl-CoA levels as key to ER homeostasis.

Introduction

The ER is the site of biosynthesis for lipids, including sterols, glycerophospholipids, and sphingolipids. The flux through the different biosynthetic pathways varies with cellular needs for different lipids and with the availability of synthetic precursors. During such fluctuations, cells must maintain ER lipid homeostasis to maintain ER structure and function and, ultimately, cell viability.

A number of protective mechanisms have evolved to ensure ER lipid homeostasis. For example, sterol levels are maintained by mechanisms that include transcriptional regulation (by sterol regulatory element-binding proteins) and posttranslational ER-associated degradation of sterol synthesis enzymes such as 3-hydroxy-3-methylglutaryl-coenzyme A (HMG-CoA) reductase (Goldstein et al., 2006). In addition, ER-localized enzymes such as acyl-CoA:cholesterol acyltransferase (ACAT) and acyl-CoA:diacylglycerol acyltransferase (DGAT) protect against the accumulation of excess free sterols or diacylglycerols (DAGs) by synthesizing cholesterol esters and triacylglycerols (TGs), respectively (Chang et al., 2009; Yen et al., 2008). These neutral lipids are subsequently removed from the ER via packaging into cytosolic lipid droplets (LDs) for storage (Walther et al., 2017). When ER-protective mechanisms are absent or overwhelmed, bioactive lipids, such as saturated glycolipids, can accumulate

and trigger stress responses (e.g., the “unfolded protein response” [Volmer and Ron, 2015]) that attempt to restore ER homeostasis (Shimabukuro et al., 1998; Unger and Zhou, 2001; Chitraju et al., 2017; Piccolis et al., 2019).

The evolutionarily conserved fat-inducing transcript (FIT) proteins, FIT1 and FIT2, have emerged as potentially important factors in ER homeostasis. These proteins encode 292-aa and 262-aa proteins, respectively, that are 35% identical and are integral ER membrane proteins with six transmembrane domains. FIT2 is expressed broadly in many tissues, including adipose tissue, whereas FIT1 is mainly expressed in skeletal muscle and heart (Kadereit et al., 2008). FIT2 was originally identified as a transcript induced by peroxisome proliferator-activated receptor- α agonists (Kadereit et al., 2008) and was subsequently shown to be important for LD formation (Kadereit et al., 2008; Moir et al., 2012; Choudhary et al., 2015). Depletion of FIT2 leads to reduced numbers of cellular LDs (Kadereit et al., 2008; Choudhary et al., 2015), and overexpression of FIT2 results in increased lipid storage in LDs (Kadereit et al., 2008; Gross et al., 2010, 2011). These changes were reported to be independent of effects on TG synthesis (Kadereit et al., 2008), suggesting that TG packaging for storage is impaired. Indeed, human FIT2 protein purified in detergent binds TG and DAG

¹Department of Molecular Metabolism, Harvard T.H. Chan School of Public Health, Boston, MA; ²Department of Cell Biology, Harvard Medical School, Boston, MA; ³Clayton Foundation Laboratories for Peptide Biology, Salk Institute for Biological Studies, La Jolla, CA; ⁴Image and Data Analysis Core, Harvard Medical School, Boston, MA; ⁵Center for Cellular and Molecular Imaging, Department of Cell Biology, Yale School of Medicine, New Haven, CT; ⁶Departments of Medicine and Pharmacology and Cancer Biology, Sarah W. Stedman Nutrition and Metabolism Center and Duke Molecular Physiology Institute, Duke University, Durham, NC; ⁷Broad Institute of MIT and Harvard, Cambridge, MA; ⁸Howard Hughes Medical Institute, Boston, MA.

*T.C. Walther and R.V. Farese Jr. contributed equally to this paper; Correspondence to Tobias C. Walther: twalther@hsph.harvard.edu; Robert V. Farese Jr.: robert@hsph.harvard.edu.

© 2020 Becuwe et al. This article is distributed under the terms of an Attribution-Noncommercial-Share Alike-No Mirror Sites license for the first six months after the publication date (see <http://www.rupress.org/terms/>). After six months it is available under a Creative Commons License (Attribution-Noncommercial-Share Alike 4.0 International license, as described at <https://creativecommons.org/licenses/by-nc-sa/4.0/>).

in vitro (Gross et al., 2011), leading to a model in which FIT2 partitions neutral lipids for LD formation (Kadereit et al., 2008; Gross et al., 2011). More recently, FIT2 and its orthologues in yeast, *Scs3* and *Yft2*, were implicated in the directionality of LD budding (Choudhary et al., 2015), possibly by regulating DAG levels at sites of LD formation (Choudhary et al., 2018).

Other evidence suggests that FIT2 functions in ER lipid metabolism more broadly than LD formation. Genetic studies of the yeast orthologues of FIT2, *SCS3* and *YFT2*, showed synthetic-genetic interactions (e.g., with *CHO2*, *OPI3*) suggesting functions in phospholipid metabolism (Moir et al., 2012). Moreover, *scs3Δ* cells are auxotrophic for inositol, a condition exacerbated by addition of choline, both key precursors in phospholipid synthesis (Hosaka et al., 1994). Consistent with the notion that FIT2 may have a role in ER phospholipid metabolism, homology searches indicate that yeast *Scs3* and *Yft2* are related to lipid phosphatase/phosphotransferase enzymes that catalyze the hydrolysis or transfer of lipid phosphate groups (Hayes et al., 2018). On the basis of these homologies, the putative active site histidines of FIT2 were shown to be required for FIT2 function in yeast (Hayes et al., 2018), although a biochemical activity for FIT2 was not identified.

Highlighting FIT2's importance, deletion of FIT2-encoding genes in organisms causes dramatic phenotypes. Deletion of the FIT2 orthologue in *Caenorhabditis elegans* is lethal (Choudhary et al., 2015), and global postnatal knockout (KO) of FIT2 in mice also results in lethality due to catastrophic intestinal effects (Goh et al., 2015). FIT2 is expressed at relatively high levels in adipose tissue (Kadereit et al., 2008), and the selective KO of murine FIT2 in adipose tissue leads to progressive lipodystrophy (Miranda et al., 2014). In humans, homozygous FIT2 deficiency was reported as a cause of deafness-dystonia (Zazo Seco et al., 2017).

Taken together, these previous studies suggest that FIT2 may be an enzyme in the ER of unknown activity that is crucial for ER lipid metabolism and ER-lipid homeostasis. In the present study, we identify the biochemical activity of FIT2 as an acyl-CoA diphosphatase of the ER and show that this activity is crucial for normal ER.

Results

FIT2 is a fatty acyl-CoA diphosphatase

Consistent with a recent study of FIT2 and its yeast orthologues (Hayes et al., 2018), we found similarity of the FIT2 amino acid sequence and overall architecture with lipid phosphate phosphatases (LPP enzymes; Figs. 1 A and S1 A). The catalytic residues of LPP enzymes are present at analogous positions in FIT2 and its yeast orthologues *Scs3* and *Yft2* (Figs. 1 A and S1 A). This includes two histidines contained in two catalytic motifs, designated C2 and C3, that are conserved across species (Fig. 1 B). The histidine at the C3 equivalent position (H214 for FIT2 and H350 for *Scs3*) is predicted to act as a nucleophile on the phosphorus of the phospholipid substrate, forming a phosphohistidine intermediate (Sigal et al., 2005). The histidine at the C2 equivalent position (H155 for FIT2 and H235 for *Scs3*) participates in the second step of the reaction and is predicted to be

involved in the hydrolysis of the phosphohistidine intermediate, leading to release of the dephosphorylated substrate. A C1 domain (KXXXXXXXXRP) that is found in most LPP enzymes and is thought to play a role in substrate recognition is not present in FIT2 proteins (Fig. 1 A). With the current model of FIT2's membrane topology (Gross et al., 2010), the putative catalytic C2 and C3 histidine residues map to the interface of the luminal ER membrane leaflet and the ER lumen (Fig. 1 C).

To determine if FIT2 has LPP activity, we used an unbiased biochemical approach to identify endogenous FIT2 substrates and products. We incubated radiolabeled [¹⁴C]oleoyl-CoA with microsomes purified from human cells overexpressing either FIT2 WT or FIT2-carrying mutations of histidines 155 and 214 to alanines (FIT2 HHAA; Fig. S1 B). TLC analysis of lipids generated in these reactions showed the rapid synthesis of a polar lipid, designated lipid 1, that was present at much higher levels with the WT than the mutant enzyme (Fig. 1 D). We also detected another, less polar lipid, designated lipid 2, that appeared in reactions containing WT but not mutant FIT2-expressing microsomes. Lipid 2 was better separated from other labeled lipids with a solvent system resolving neutral lipids (Fig. 1 E). Both lipids 1 and 2 were relatively short-lived in microsomes. Their levels peaked ~10 min after adding radiolabeled oleoyl-CoA, and by 60 min, both lipids were markedly reduced, likely due to their further metabolism in microsomes. However, both lipids were regenerated by re-adding labeled oleoyl-CoA to the reaction after 60 min (Fig. 1, D and E).

To determine the identities of lipids 1 and 2, we used mass spectrometry (MS) to analyze lipid extracts from microsomes of cells overexpressing either WT FIT2 or FIT2 HHAA incubated with oleoyl-CoA or palmitoyl-CoA for 10 or 30 min. We set three criteria for the identification of these lipids. First, both lipids should accumulate in microsomes overexpressing FIT2 WT but not FIT2 HHAA. Second, their levels should be more abundant at 10 min than at 30 min. Third, they should have a 26-D mass shift in the samples incubated with oleoyl-CoA versus palmitoyl-CoA (corresponding to the two additional carbons and hydrogens in the oleoyl-CoA acyl chains).

We identified two lipids satisfying these criteria. These ions had respective masses of 621.335 and 543.383 D in oleoyl-CoA-treated samples (Fig. 1, F-H) and 595.318 and 517.367 D in palmitoyl-CoA-treated samples (Fig. S1 C). Their fragmentations resulted in ion series corresponding to oleoyl 4'-phosphopantetheine (Fig. 1 F) and oleoyl pantetheine (Fig. 1 H) for oleoyl-CoA-treated samples and palmitoyl 4'-phosphopantetheine and palmitoyl pantetheine for palmitoyl-CoA-treated samples in cells expressing FIT2 WT (Fig. S1 C). The levels of these lipids were higher at 10 min than at 30 min and nearly absent in FIT2 HHAA-overexpressing microsomes (Fig. 1, G-I; Fig. S1 C). On the basis of these findings, we hypothesized that lipid 1 is acyl 4'-phosphopantetheine and lipid 2 is acyl pantetheine. These lipids differ by one phosphate group, which can explain their different migration observed by TLC.

On the basis of the structure of the molecules, possible precursors for their synthesis are acyl-CoAs. To directly test whether FIT2 catalyzes the cleavage of acyl-CoA to acyl 4'-phosphopantetheine and adenosine-3',5'-bisphosphate, we

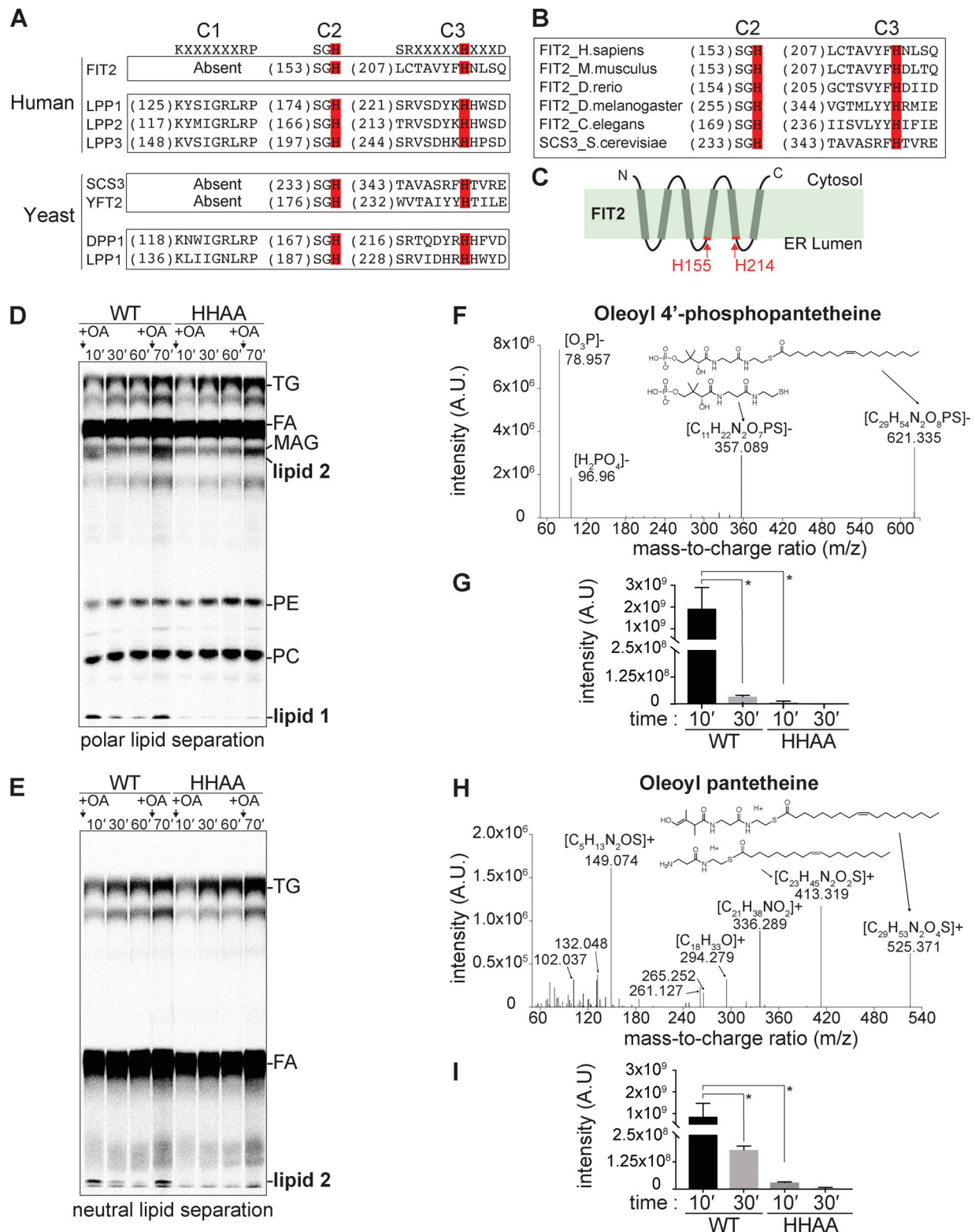


Figure 1. **FIT2 overexpression in microsomes increases levels of oleoyl 4'-phosphopantetheine and oleoyl pantetheine upon oleoyl-CoA incubation.** (A) FIT2 shares conserved motifs with LPP enzymes. C1, C2, and C3 motifs were aligned using human and yeast LPP members. FIT2 and its yeast homologues Scs3 and Yft2 have two conserved LPP motifs, C2 and C3. The conserved catalytic histidines are highlighted in red. (B) C2 and C3 catalytic histidines (highlighted in red) are evolutionarily conserved within FIT2 sequences. (C) On the basis of topology analysis (Gross et al., 2010), FIT2 N- and C-termini are predicted to be cytosolic, and the C2 and C3 motifs are predicted to be oriented toward the ER lumen. Transmembrane domains are represented as gray bars. Red boxes represent the C2 and C3 catalytic histidines. (D and E) Overexpression of FIT2 yields the production of lipids 1 and 2 upon oleoyl-CoA loading. Purified microsomes from human GnTi- 293 cells overexpressing FIT2 WT or mutated for C2 and C3 histidine to alanine (H155A and H214A, HHAA) were loaded with 25 μ M mixed unlabeled and radiolabeled [14 C]oleoyl-CoA, and lipids were extracted at different time points. Oleoyl-CoA was added a second time after

60 min for 10 min. Lipids were separated on a silica plate by TLC using solvents to separate polar (D) or neutral lipids (E). Autoradiograph of one representative TLC for each type of solvent is shown. OA, oleoyl coenzyme A; FA, free oleic acid; MAG, monoacylglycerol; PC, phosphatidylcholine; PE, phosphatidylethanolamine. **(F–I)** Identification of lipids 1 and 2 by MS. Lipids from a microsomal extract overexpressing either FIT2 WT or FIT2 HHAA loaded with oleoyl-CoA for 10 and 30 min were analyzed by MS. Fragmentation pattern of ions 621.335 D and 525.371 D, corresponding to (F) oleoyl 4'-phosphopantetheine and (H) oleoyl pantetheine, respectively, as well as the structures assigned for each main peak, are presented. Bar graphs showing intensity level of these metabolites (G and I) found in microsomes overexpressing FIT2 WT or FIT2 HHAA at two different time points after oleoyl-CoA loading (10 and 30 min) are presented. Mean values \pm SD, two-way ANOVA with Sidak test. *, $P < 0.0001$.

incubated recombinantly produced human FIT2 WT or FIT2 HHAA proteins (Figs. 2 A and S1 D) with oleoyl-CoA and analyzed reaction products by TLC. At 10 or 30 min, FIT2 WT, but not FIT2 HHAA, produced lipid 1, but not lipid 2 (Fig. 2 B). To confirm the identity of lipid 1, we purified lipid 1 from the TLC silica plate. MS revealed the presence of an ion with a mass of 623.335 D only in the lipid extract from the FIT2 WT assay (Fig. 2 C). This ion was not found in lipids extracted from assays with recombinant FIT2 HHAA protein or from a blank silica control (Fig. 2, D and E). Higher-energy collision dissociation of this parent ion yielded a mass spectrum consistent with oleoyl 4'-phosphopantetheine fragmentation (Fig. 2 F). In this experiment, this ion was only detected by MS in positive mode and therefore shows a mass difference of 2 D (for two protons) compared with the ion found in the microsomal extract analysis that identified oleoyl 4'-phosphopantetheine in negative mode (Fig. 1 F).

To test whether oleoyl pantetheine (lipid 2) was produced by another enzyme in the microsomal extract, we incubated recombinant FIT2 WT protein with oleoyl-CoA for 60 min to produce oleoyl 4'-phosphopantetheine, and we then added microsomes from WT cells to the reaction. Under these conditions, the oleoyl 4'-phosphopantetheine produced by recombinant FIT2 was metabolized to other lipids, including oleoyl pantetheine (Fig. 2 G), showing that dephosphorylation of oleoyl 4'-phosphopantetheine occurs through a separate activity in the microsomal fractions. This was not the case when oleoyl-CoA was preincubated with recombinant FIT2 HHAA protein, suggesting that oleoyl pantetheine can be made from oleoyl 4'-phosphopantetheine but not from oleoyl-CoA directly. To confirm that oleoyl pantetheine is produced by an enzyme independent of FIT2, we incubated oleoyl 4'-pantetheine with microsomes purified from FIT2 WT or FIT2-KO cells. Either microsome preparation was capable of generating the same lipid products (Fig. S1 E), including acyl pantetheine, indicating that the acyl 4'-phosphopantetheine dephosphorylation is performed by a different enzyme.

In biochemical experiments with oleoyl-CoA as substrate, recombinant FIT2 had diphosphatase activity with an apparent K_m of 10 μ M and a V_{max} of 6.5 μ mol/min/mg (Fig. 3, A–C). Comparing the substrate specificities of FIT2, we found that saturated long-chain fatty acyl-CoAs [stearoyl-CoA (18:0), arachidoyl-CoA (20:0)] competed poorly with oleoyl-CoA as a substrate, although saturated fatty acyl-CoAs with shorter fatty acid chains [palmitoyl-CoA (16:0)] competed better (Fig. 3 D). Polyunsaturated long-chain fatty acyl-CoA [arachidonoyl CoA (20:4)] exhibited higher levels of competition (Fig. 3 D). Acetyl-CoA did not compete with oleoyl-CoA and appeared not to be an FIT2 substrate.

We also tested whether the enzyme displays activity against known LPP substrates, such as lysophosphatidic acid and phosphatidic acid. However, we found low affinity and slow catalytic rates of FIT2 with these substrates, suggesting that they were not the primary substrates of FIT2 in cells (Becuwe et al., 2018).

To further test the hypothesis that FIT2 is an acyl-CoA diphosphatase, we measured acyl-CoA levels in FIT2-KO cells by MS. Oleoyl-CoA and arachidonoyl-CoA were the only detected fatty acyl-CoAs, and levels of both species were increased in FIT2-KO cells compared with WT cells (Fig. 3 E), consistent with both being substrates for the enzyme (Fig. 3 D). CoA and acetyl-CoA levels were similar in WT and FIT2-KO cells, indicating that FIT2 deficiency does not deplete these metabolites in these cells.

Together, these data demonstrate that FIT2 is a diphosphatase cleaving the phosphoanhydride bond of acyl-CoA to yield acyl 4'-phosphopantetheine and adenosine-3',5'-bisphosphate. Acyl 4'-phosphopantetheine is subsequently dephosphorylated by a different activity, present in microsomes, to acyl pantetheine (Fig. 3 F). FIT2 appears to have preference for unsaturated long-chain acyl-CoA substrates.

FIT2 deficiency in mammalian cells impairs ER morphology

To study FIT2 function in ER lipid metabolism in human cells, we generated a FIT2-KO human SUM159 cell line. Sequencing the FIT2 alleles of the KO cells showed a homozygous 17-bp deletion at the junction of exon 1 and the first intron (designated clone 1; Fig. S2 A). The mutation yielded markedly reduced FIT2 mRNA expression and undetectable FIT2 protein (Fig. S2, B and C). Compared with the reticular pattern of ER in WT cells, FIT2-KO cells exhibited dramatically altered ER morphology, as visualized by expressing ER marker proteins (Fig. 4 A). The ER was often found in clumps, suggesting aggregated membranes. Ultrastructural analyses of FIT2-KO cells by thin-section EM showed that these cells had abundant whorls of membranes (Fig. 4 B) in the majority (39 of 71) of EM thin sections. Membrane whorls were never found in WT cells. The whorls appeared to be ER membranes because many ribosomes were attached. FIT2-KO cells also exhibited frequent occurrences of dilated ER (Fig. 4 C). Using lattice light-sheet microscopy of cells expressing a fluorescent ER marker, we found that the ER clumps in FIT2-KO cells were typically located close to the nuclear envelope and reached up to 5 μ m in diameter and 20 μ m³ in volume (Fig. 4 D). Moreover, no colocalization between these ER clumps and the autophagy marker LC3 was detected (Fig. S3 A), suggesting that the ER aggregates observed in FIT2-KO cells were not encapsulated in autophagosomes. We also tested whether overexpression of reticulons, which induce the formation of tubules in the ER (Voeltz et al., 2006), could resolve

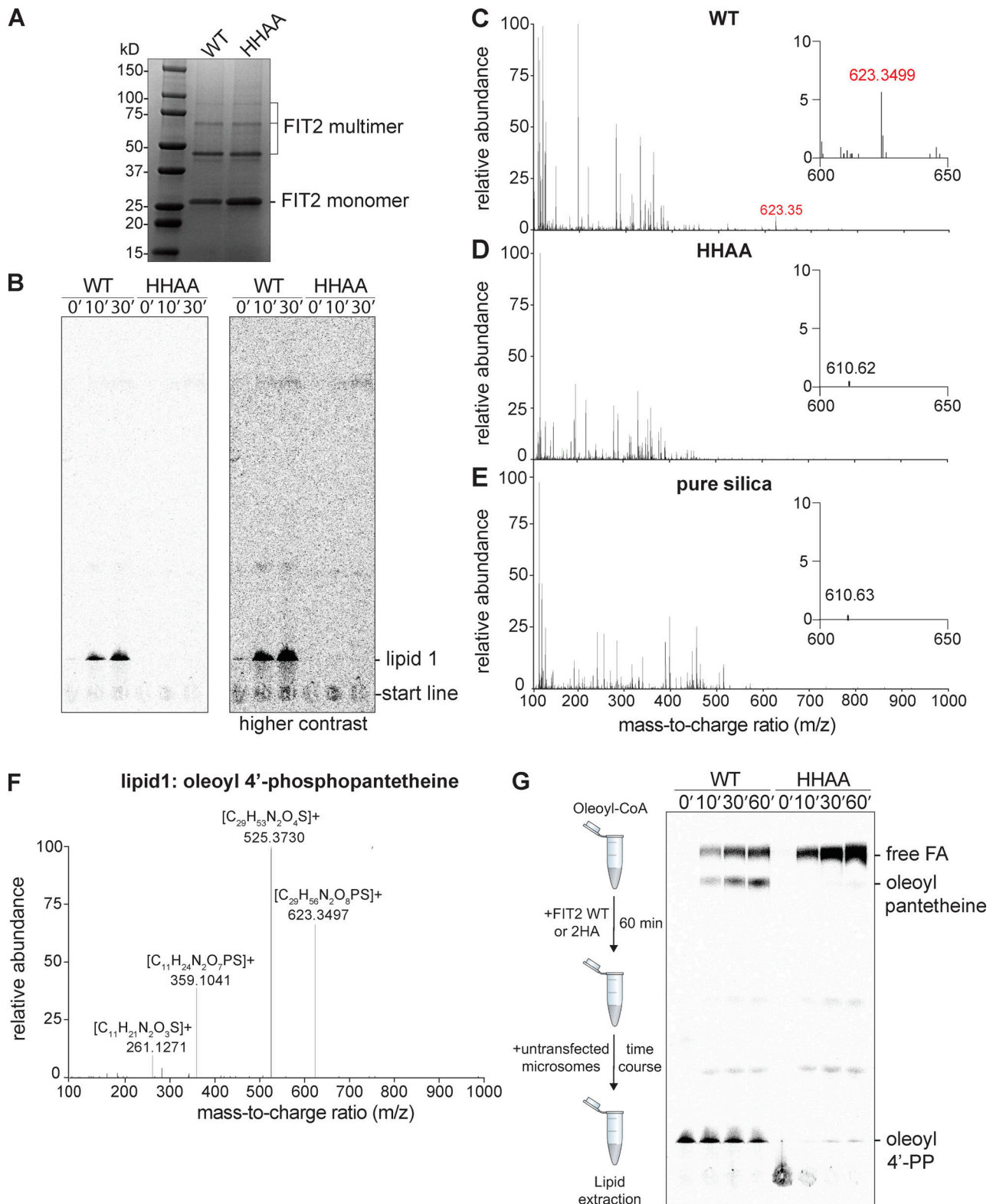


Figure 2. **Recombinant human FIT2 catalyzes the cleavage of oleoyl-CoA to oleoyl 4'-phosphopantetheine but not oleoyl pantetheine.** (A) Coomassie blue-stained SDS-PAGE analysis of recombinant FIT2 WT and HHAA protein purified from GnTI- 293 cells. FIT2 protein forms multimers, as confirmed by Western blot analysis (Fig. S1D). (B) Incubation of oleoyl-CoA with FIT2 WT protein produces lipid 1. 25 ng of recombinant FIT2 WT or HHAA was incubated for the indicated time with 25 μ M mixed unlabeled and radiolabeled [14 C]oleoyl-CoA, and lipids produced during the reaction were analyzed by TLC using the solvent for polar lipids. A more contrasted image of the TLC is also shown. (C–E) Similar assay as that in B with FIT2 WT protein was performed with unlabeled oleoyl-CoA, and the silica plate was scraped at the location of lipid 1 (C). Reactions with FIT2 HHAA protein (D) or an empty silica lane (E) were used as controls. After extraction, lipids were directly infused into a mass spectrometer, and measured spectra are presented. (F) Fragmentation pattern after higher-energy

collision dissociation of the ion 623.3499 D identified in C. **(G)** Incubation of oleoyl-CoA with FIT2 WT protein produces oleoyl 4'-phosphopantetheine but not oleoyl pantetheine. Schematic representation of the experiment is shown on the left. Recombinant FIT2 WT or HHA was incubated for 60 min with mixed unlabeled and radiolabeled [¹⁴C]oleoyl-CoA, and then microsomes purified from WT Gnt1⁻ 293 cells were added and incubated for the indicated time. Lipids were separated by TLC with polar lipid solvent. Oleoyl 4'-PP, oleoyl 4'-phosphopantetheine.

the ER aggregates. However, we did not detect any changes of the ER clumps upon overexpression of RTN4a (Fig. S3 B). In contrast to the prominent effects of FIT2 deficiency on the ER, we found no differences in the appearance of the Golgi apparatus, lysosomes, or peroxisomes (Fig. S3 C). Similar ER phenotypes were found in a second FIT2-KO cell line (clone 2), which is compound heterozygous (with one allele harboring a large deletion of *FIT2* coding sequence and the second allele encoding a protein lacking a single aa), leading to greatly reduced expression of *FIT2* (~20% of *FIT2* mRNA left as determined by quantitative PCR [qPCR] analysis; Fig. S2, A–D).

The ER whorls in FIT2-KO cells are reminiscent of membrane whorls observed during unresolved ER stress in yeast (Schuck et al., 2009). Activation of the unfolded protein response triggers the upregulation of a large set of ER proteins, including phospholipid synthesis enzymes that provide more membrane lipids. Although we did not detect changes in Xbp1 splicing (a marker of acute ER stress), mRNA levels of ATF3, BiP, and CHOP were modestly upregulated in *FIT2*-KO cells cultured under basal conditions and were further increased with palmitate addition (Fig. 4, E and F), which increases lipotoxic stress. Consistent with moderate activation of ER stress-sensing pathways, *FIT2*-KO cells showed increased protein levels of BiP and inositol-requiring enzyme 1 α (IRE1 α ; Fig. 4 G). In contrast, we did not detect increased phosphorylation of eIF2 α , suggesting that the PKR-like endoplasmic reticulum kinase pathway is not constitutively activated in *FIT2*-KO cells.

To examine the acute rather than chronic effects of *FIT2* deficiency on ER morphology, we depleted *FIT2* by RNA interference. *FIT2* mRNA levels were 90% lower after 72 h of siRNA treatment (Fig. S4, A and B). In agreement with an acute effect of *FIT2* deficiency on ER morphology, these *FIT2*-knockdown (*FIT2*-KD) cells exhibited a higher proportion of ER sheets in the cell periphery (Fig. 4, H and I; Fig. S4 C). We also examined whether ER stress was induced upon acute *FIT2* depletion in cells. However, no activation of ER stress was detected in *FIT2*-KD cells (Fig. 4 J), possibly due to the lack of activation at the time sampled.

FIT2 is required for normal LD formation and glycerolipid synthesis in mammalian cells

We next examined *FIT2* function with respect to LD formation in mammalian cells. We first observed *FIT2* localization during LD formation in cells expressing a CRISPR-engineered (endogenous N-terminal GFP-tagged) *FIT2* (Fig. S4 D). *FIT2* displayed a diffuse signal that colocalized with the ER marker signal sequence BFP-KDEL, and this localization appeared unchanged during LD formation (Fig. 5 A).

We next examined LD formation in *FIT2*-KO cells. Consistent with the notion that *FIT2* function is required for normal LD formation, incubation of *FIT2*-KO cells in medium containing

oleate resulted in the formation of fewer LDs at each time point than in control cells (Fig. 5, B and C). To determine if the reduction in LD numbers was due to altered synthesis of TG or a defect in LD biogenesis, we measured TG synthesis by including a radioactive tracer ([¹⁴C]oleate) in the oleate-containing medium. *FIT2* deletion impaired TG synthesis compared with WT cells (Fig. 5 D), similar to what was reported in mouse 3T3-L1 cells with *FIT2* knockdown (Kadereit et al., 2008). However, despite the neutral lipid synthesis defect, *FIT2* deficiency resulted in fewer LDs formed normalized to the amount of synthesized TG (Fig. 5 E). Thus, *FIT2* depletion has an effect on LD formation that is independent of TG synthesis per se, in agreement with a previous report (Kadereit et al., 2008). Similar LD-related phenotypes were found in the second clonal *FIT2*-KO cell line (Fig. S2, E–G).

We also detected a similar delay in LD formation in yeast when both *SCS3* and *YFT2* were deleted. In yeast, four genes encode the enzymes of neutral lipid synthesis (Dahlqvist et al., 2000; Oelkers et al., 2000, 2002; Sorger and Daum, 2002): *DGA1* and *LRO1* generate TG, and *ARE1* and *ARE2* primarily synthesize sterol ester. We used a yeast strain in which *LRO1* and *ARE1* were deleted and where *DGA1* and *ARE2* were placed under the control of a galactose-inducible promoter. This strain, designated as “inducible LD,” enabled us to induce LD formation by switching cells from raffinose- to galactose-containing medium (similar to the strain used by Cartwright et al., 2015). After induction, we found that the formation of LDs, assessed by BODIPY staining, was delayed by deletion of *SCS3* and *YFT2* (Fig. S5, A and B).

To determine the effects of *FIT2* depletion on the expression of lipid synthesis genes, we measured the mRNA expression of genes involved in TG synthesis by qPCR. No differences were found for most of the glycerol-phosphate acyltransferase (GPAT) and acylglycerol-phosphate acyltransferase (AGPAT) enzymes, but the mRNA levels for *LIPIN1*, *DGAT1*, and *DGAT2* were markedly reduced in *FIT2*-KO cells (Fig. 5 F). In contrast, *AGPAT3* mRNA levels were increased. We also examined gene expression after acute *FIT2* knockdown. As in the *FIT2*-KO cells, *LIPIN1* and *DGAT1* mRNA levels were reduced in *FIT2*-KD cells (Fig. 5 G). *GPAT3* and *AGPAT3* mRNA levels were increased. However, in contrast to *FIT2*-KO cells, *DGAT2* mRNA levels were similar in *FIT2*-KD and control cells, consistent with the hypothesis that *DGAT2* expression is downregulated in *FIT2*-KO cells as an adaptation to long-term *FIT2* deletion. Similar to *FIT2*-KO cells, *FIT2*-KD cells formed smaller LDs (Fig. 5 H), further confirming that *FIT2* is required for efficient LD formation.

FIT2 catalytic residues are required for ER homeostasis in yeast

Because the deletion of the *FIT2* yeast homologue *SCS3* has been well characterized (Hosaka et al., 1994; Choudhary et al., 2015; Hayes et al., 2018), we performed studies in *Saccharomyces*

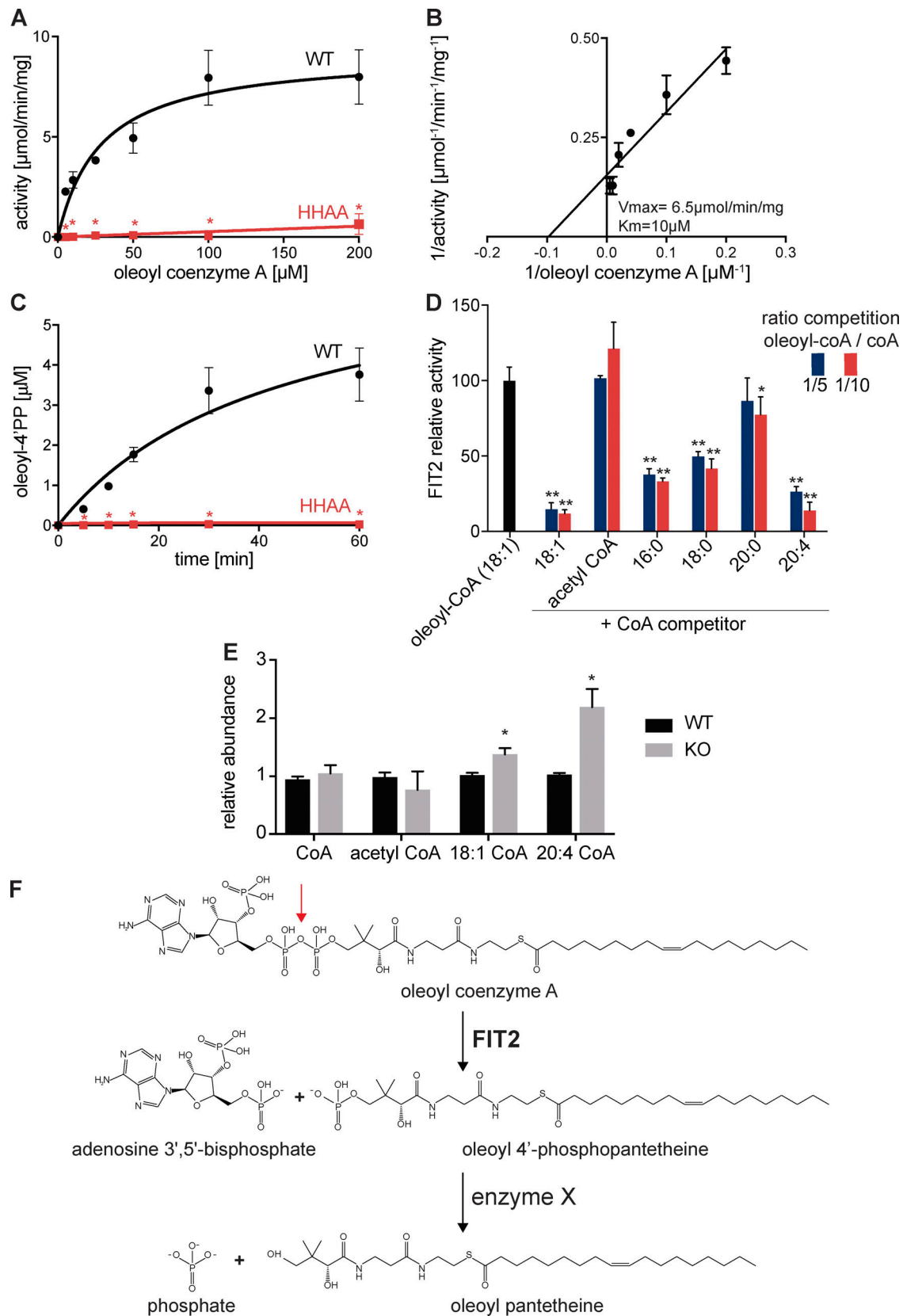


Figure 3. **Characterization of acyl-CoA diphosphatase activity of human FIT2.** (A–C) FIT2 has oleoyl-CoA diphosphatase activity. Oleoyl-CoA diphosphatase activity was measured by the formation of oleoyl 4'-phosphopantetheine, analyzed by TLC. (A) Substrate-dependent oleoyl-CoA diphosphatase assay. The indicated concentration of mixed unlabeled and radiolabeled [^{14}C]oleoyl-CoA was incubated for 10 min with 25 ng of purified FIT2 WT or FIT2 HHAA. The amount of oleoyl 4'-phosphopantetheine produced for each oleoyl-CoA concentration was quantified from triplicate experiments, and mean values \pm SD were

plotted against the oleoyl-CoA concentration (two-way ANOVA with Sidak test; *, $P < 0.0001$). (B) Same data as in A plotted as a Lineweaver-Burk diagram with V_{max} and K_m . (C) Time-dependent oleoyl-CoA diphosphatase assay. 5 μM of mixed unlabeled and radiolabeled [^{14}C]oleoyl-CoA was incubated with 10 ng of WT FIT2 for the indicated time. The amounts of oleoyl 4'-phosphopantetheine produced at each time point were quantified, and mean values \pm SD were plotted over time (two-way ANOVA with Sidak test; *, $P < 0.0001$). (D) Oleoyl-CoA is FIT2's preferential substrate. 25 ng of purified FIT2 WT protein were incubated for 10 min with a mix of unlabeled and radiolabeled [^{14}C]oleoyl-CoA (5 μM) and unlabeled CoA competitor (25 μM for ratio of 1:5 or 50 μM for ratio of 1:10). FIT2 activity was calculated relative to its activity with radiolabeled oleoyl-CoA alone. Mean values \pm SD from triplicate measurements are presented in a bar graph (two-way ANOVA with Tukey test; **, $P < 0.0001$; *, $P < 0.05$). (E) Oleoyl-CoA and arachidonoyl-CoA levels are increased in FIT2-KO cells. Levels of CoA, acetyl-CoA, oleoyl-CoA, and arachidonoyl-CoA in total cell lysates from FIT2 WT and FIT2-KO cells pretreated with oleic acid for 90 min (mean values \pm SD, t test; *, $P < 0.01$). (F) FIT2 cleaves the oleoyl-CoA phosphoanhydride bond (red arrow) to produce oleoyl 4'-phosphopantetheine and 3'-5'-ADP. Another microsomal enzyme hydrolyzes oleoyl 4'-phosphopantetheine to yield oleoyl pantetheine. Chemical structures are presented.

cerevisiae to test whether the acyl-CoA diphosphatase activity of FIT2 is crucial for its function in vivo. In agreement with a role in lipid metabolism, SCS3 was required for inositol prototrophy (Hosaka et al., 1994; Fig. 6 A). This phenotype was complemented by introducing either WT Scs3 or human FIT2 (Figs. 6 A and S5 C), showing that this FIT2 function is evolutionarily conserved from yeast to humans. Adding back mutant forms of these enzymes (Scs3 H235A or Scs3 H350A; FIT2 H155A or FIT2 H214A) failed to restore growth on media lacking inositol (Fig. 6 A), showing that FIT2 catalytic residues are crucial for this phenotype in vivo.

Because inositol has a key role in yeast phospholipid metabolism, we next asked whether SCS3 deletion impacts ER membrane homeostasis. Indeed, in the absence of Scs3, cells had abundant clumps of ER membrane (Fig. 6 B). This phenotype was complemented by expressing WT Scs3, but not by expressing mutant forms of the protein (scs3 H235A or scs3 H350A; Fig. 6 C). The ER phenotype was also complemented by expressing human FIT2 WT in *scs3* Δ cells, but not by expressing catalytically deficient FIT2 (FIT2 H155A or FIT2 H214A; Fig. 6 D). Also, the introduction of either Scs3 histidine mutant into a WT strain did not induce the formation of ER clumps or complement the inositol auxotrophy (Fig. S5, D and E), indicating that expression of those mutants does not have dominant-negative effects. Overall, these data indicate that the catalytic residues, and thus likely the FIT2 acyl-CoA diphosphatase activity, are required for its ER-related function.

FIT2 activity is required for ER homeostasis and normal lipid storage in mammalian cells

We tested whether FIT2 activity is required for ER homeostasis in mammalian cells by performing add-back experiments in the FIT2-KO cell lines. Expression of FIT2 WT, but not catalytic mutant forms, completely reversed the ER morphology phenotype associated with FIT2 deletion (Fig. 7, A and B). This rescue of ER morphology correlated with normalization of several ER stress markers. Adding back FIT2 WT, but not the catalytically mutant form of FIT2, partially restored ATF3 and BiP mRNA levels (Fig. 7 C) and BiP and inositol-requiring enzyme 1 protein levels (Fig. 7 D).

We asked whether restoring FIT2 activity would reverse the changes in lipid gene expression by stably reintroducing WT or catalytic mutant (H214A) FIT2 into FIT2-KO cells (Fig. S4 E). However, neither the changes in gene expression nor the TG synthesis rates were normalized (Fig. 7, E and F), suggesting that the changes in gene expression and TG synthesis occur as a

secondary consequence of long-term FIT2 depletion in cells. In contrast to the studies on expression of lipid synthesis genes, reintegration of FIT2 WT but not FIT2 H214A in FIT2-KO cells restored normal LD formation (Fig. 7 G), indicating a distinct function of FIT2 in LD formation.

Discussion

The molecular function of the ER protein FIT2 has been a mystery since its identification. Here, we show that FIT2 is an acyl-CoA diphosphatase enzyme that cleaves the phosphoanhydride bond of acyl-CoA to yield acyl 4'-phosphopantetheine and adenosine-3',5'-bisphosphate. Our conclusions are based on three lines of evidence. First, WT but not mutant FIT2 overexpression in microsomes incubated with labeled acyl-CoA leads to generation of acyl 4'-phosphopantetheine and subsequently its derivative, acyl pantetheine. Second, recombinant FIT2 efficiently cleaves the phosphoanhydride bond of acyl-CoA in vitro, yielding acyl 4'-phosphopantetheine as a product. The affinity for the substrate is comparable with the cellular concentration of fatty acyl-CoAs, which are likely found at low micromolar or nanomolar concentrations (Grevengoed et al., 2014; Naquet et al., 2020). Third, deletion of FIT2 in mammalian cells results in increased levels of acyl-CoA substrates. Taken together, our data identify hydrolysis of fatty acyl-CoAs, in particular unsaturated acyl-CoA species, as the primary function of FIT2.

The acyl-CoA hydrolysis activity of FIT2 appears to be localized to the ER lumen. Previous studies showed that the conserved catalytic histidine residues are predicted to be localized to the luminal side of the ER bilayer (Gross et al., 2010). Acyl-CoAs are produced in the cytosol by acyl-CoA synthetase long-chain proteins (Soupe and Kuypers, 2008). How would acyl-CoAs reach the ER lumen? Others have reported that the ER has an ER-localized acyl carnitine transferase activity similar to the mitochondria (Gooding et al., 2004). To our knowledge, acyl-CoA hydrolases have not been reported in the ER lumen, suggesting that FIT2 activity evolved to help prevent buildup of fatty acyl-CoAs on the luminal leaflet of the ER.

The current data support the hypothesis that accumulation of acyl-CoA substrates rather than reaction products leads to cell dysfunction. In the absence of FIT2 activity, excess luminal acyl-CoAs may disrupt ER membranes, possibly by acting as detergents to destabilize membranes or by altering phospholipid balance. The reaction products of the FIT2 enzyme (acyl 4'-phosphopantetheine and adenosine-3',5'-bisphosphate) are linked to important metabolic processes (Naquet et al., 2020). It has

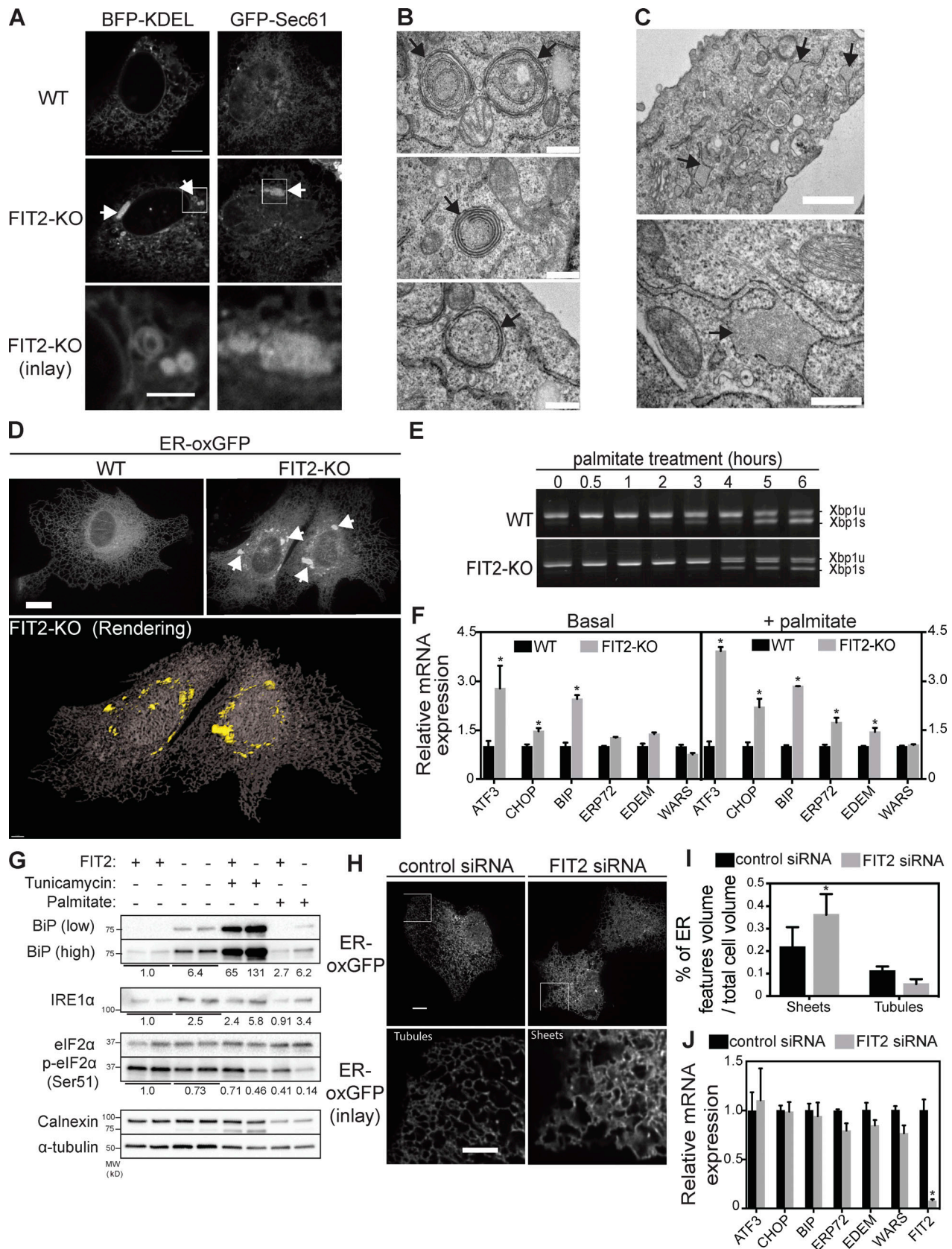


Figure 4. **FIT2-deficient human SUM159 cells have altered ER morphology.** (A) Confocal images of FIT2 WT and FIT2-KO SUM159 cells transiently expressing the ER marker ssBFP-KDEL or GFP-Sec61β. White arrows indicate ER aberrations. Scale bar = 10 μm. (B and C) Representative thin-section EM scans from FIT2-KO cells showing (B) ER whorls highlighted with black arrows (scale bars = 500 nm) and (C) ER dilation highlighted with black arrows (scale bars = 1 μm [top

image], 500 nm [bottom image]). **(D)** ER whorls in FIT2-deficient cells are localized perinuclearly. Representative lattice light-sheet microscopy images of FIT2 WT and FIT2-KO cells transiently expressing oxGFP-KDEL. ER abnormalities are indicated with white arrows. Scale bar = 10 μ m. A rendering image shows the ER meshwork (brown) and the perinuclear localization of ER whorls (yellow shapes). Scale bar = 4 μ m. **(E)** The ER stress marker XBP1 is normally regulated in FIT2-KO cells. XBP1 mRNA from FIT2 WT or FIT2-KO cells, treated for the indicated times with 100 μ M palmitate, was amplified by qPCR and loaded onto an agarose gel. Unspliced XBP1 (Xbp1u) was observed as a 152-bp band, and the spliced form (XBP1s) was observed as a 126-bp band. **(F)** Several ER stress markers are elevated in FIT2-KO cells. qPCR analysis of the indicated genes was performed on FIT2 WT and FIT2-KO cells untreated or treated with 100 μ M palmitate for 16 h. Values represent mean \pm SD relative to WT value; $n = 3$ (two-way ANOVA with Sidak test; *, $P < 0.05$). **(G)** Western blot analysis of the indicated proteins was performed on FIT2 WT and FIT2-KO cells untreated or treated with 100 μ M palmitate for 16 h or tunicamycin (4 μ g/ml) for 14 h. Quantification of band intensity relative to untreated WT controls is shown under each panel. **(H and I)** FIT2 siRNA-treated cells have more ER sheets than control siRNA-treated cells. **(H)** Confocal images of WT cells transiently expressing the ER marker oxGFP-KDEL treated with control or FIT2 siRNA for 72 h. An inlay highlights the higher proportion of sheetlike structures at the cell periphery in FIT2 siRNA-treated cells than in controls. Scale bar = 10 μ m. **(I)** Quantification of ER features (sheets and tubules) relative to the cell volume in cells treated with control siRNA or FIT2 siRNA for 3 d and transiently expressing the ER marker oxGFP-KDEL. Quantification was performed as described in the Materials and methods section (two-way ANOVA with Bonferroni test; *, $P < 0.0001$). **(J)** Knock-down of FIT2 does not induce ER stress. mRNA levels of the indicated genes were assessed by qPCR analysis of WT cells pretreated with control or FIT2 siRNA for 72 h. Values represent mean \pm SD relative to WT value; $n = 3$. The figure is representative of two independent experiments (two-way ANOVA with Sidak test; *, $P < 0.05$).

been shown that CoA deficiency induces ER dilation in mice, and this phenotype can be rescued by the addition of acetyl-4'-phosphopantetheine (Di Meo et al., 2017). However, we currently have no evidence for CoA deficiency or other alterations of cell metabolism from product deficiency in FIT2-KO cells. Nevertheless, the mechanistic link between FIT2 deficiency and ER dysfunction requires further investigation.

The diphosphatase reaction catalyzed by FIT2 is similar to that catalyzed by several nucleoside diphosphates linked to moiety-X (Nudix) hydrolase enzymes that are found in peroxisomes and mitochondria (McLennan, 2006; Kerr et al., 2019). This superfamily of enzymes hydrolyzes a wide variety of nucleoside diphosphate substrates and contains a highly conserved 23-aa sequence motif, called a "Nudix box" (Mildvan et al., 2005). This motif is not present in FIT2, indicating that FIT2 and Nudix enzymes carry out this reaction by distinct catalytic mechanisms. Nudix hydrolases 7, 8, and 19 are family members with acyl-CoA diphosphatase activity (Gasmi and McLennan, 2001; Ofman et al., 2006; Kerr et al., 2019). The function of Nudix enzymes in peroxisomes is unknown, but they were suggested to catabolize fatty acyl-CoAs, allowing breakdown products to leave the lysosome for recycling.

Our findings for FIT2 enzyme deletions in yeast and mammalian cells show that FIT2 activity is crucial for maintaining normal ER morphology. In *scs3 Δ* yeast cells, the ER exhibited major defects that were rescued by WT but not catalytic mutant versions of *Scs3* or FIT2. In our studies of mammalian cells, FIT2 deficiency similarly resulted in ER morphology defects and indicators of ER stress that were largely rescued by complementation with active forms of the enzyme. The ER defects caused by FIT2 deficiency included increased amounts of ER sheets in FIT2-KD cells and severe ER aberrations such as clumps and whorls in FIT2-KO cells. ER membrane whorls in cells have been found in different situations linked to abnormalities in lipid metabolism, such as unresolved ER stress (Schuck et al., 2009), phosphatidylcholine deficiency (Testerink et al., 2009), and increased fatty acid saturation (Surma et al., 2013). Thus, the occurrence of whorls in FIT2-deficient cells is consistent with abnormalities in the ER phospholipids.

Previous studies suggested a primary function of FIT2 in the formation of LDs: for instance, as a structural protein or as

packaging DAG and/or TG into LDs (Gross et al., 2011; Choudhary et al., 2015). Consistent with these studies, we also found that FIT2 depletion had marked effects on LD formation in both yeast and mammalian cells. In mammalian cells, we found reduced numbers of LDs formed for a given amount of TG synthesis, suggesting that LD formation is less efficient with FIT2 deletion. How might FIT2 function help maintain normal LD formation? One possibility is that FIT2-mediated hydrolysis of acyl-CoAs provides a general function in the ER lumen that helps to maintain normal phospholipid balance between the two ER leaflets that promotes normal LD budding. For example, we found that FIT2 deficiency resulted in an increased proportion of ER sheets versus tubules, and evidence suggests that ER sheets do not support LD formation as well as tubules (Santinho et al., 2020). Another possibility is that FIT2 performs a specific function that facilitates LD formation. For example, because FIT2 is known to bind neutral lipids such as DAG and TG (Gross et al., 2011) that may alter the conformation of FIT2 (Gross et al., 2010), an attractive hypothesis is that cleavage of the acyl-CoA phosphoanhydride bond could be coupled to conformational changes that produce active pumping of neutral lipids across the membrane. Such an activity could be important, for example, in reducing DAG levels in the vicinity of LD budding at the cytosolic leaflet to facilitate budding, as proposed previously (Choudhary et al., 2018). With a primary enzymatic function for FIT2 identified, this and other hypotheses can now be tested.

Materials and methods

Mammalian cell culture and transfection

Human SUM159 cells (breast carcinoma cell line) were maintained in DMEM/F-12 GlutaMAX medium (Life Technologies) containing 5% FBS, 100 U/ml penicillin, 100 mg/ml streptomycin, 1 mg/ml hydrocortisone (MilliporeSigma), 5 mg/ml insulin (Cell Applications), and 10 mM HEPES, pH 7.0. Transfection of plasmids was performed 24 h before experiments with FuGENE-HD (Promega) according to the manufacturer's instructions. siRNA treatment was performed 72 h before the experiment by reverse transfection using Lipofectamine RNAiMAX (Thermo Fisher Scientific) according to the manufacturer's instructions. Human Expi293F GnTI⁻ cells were grown in suspension in

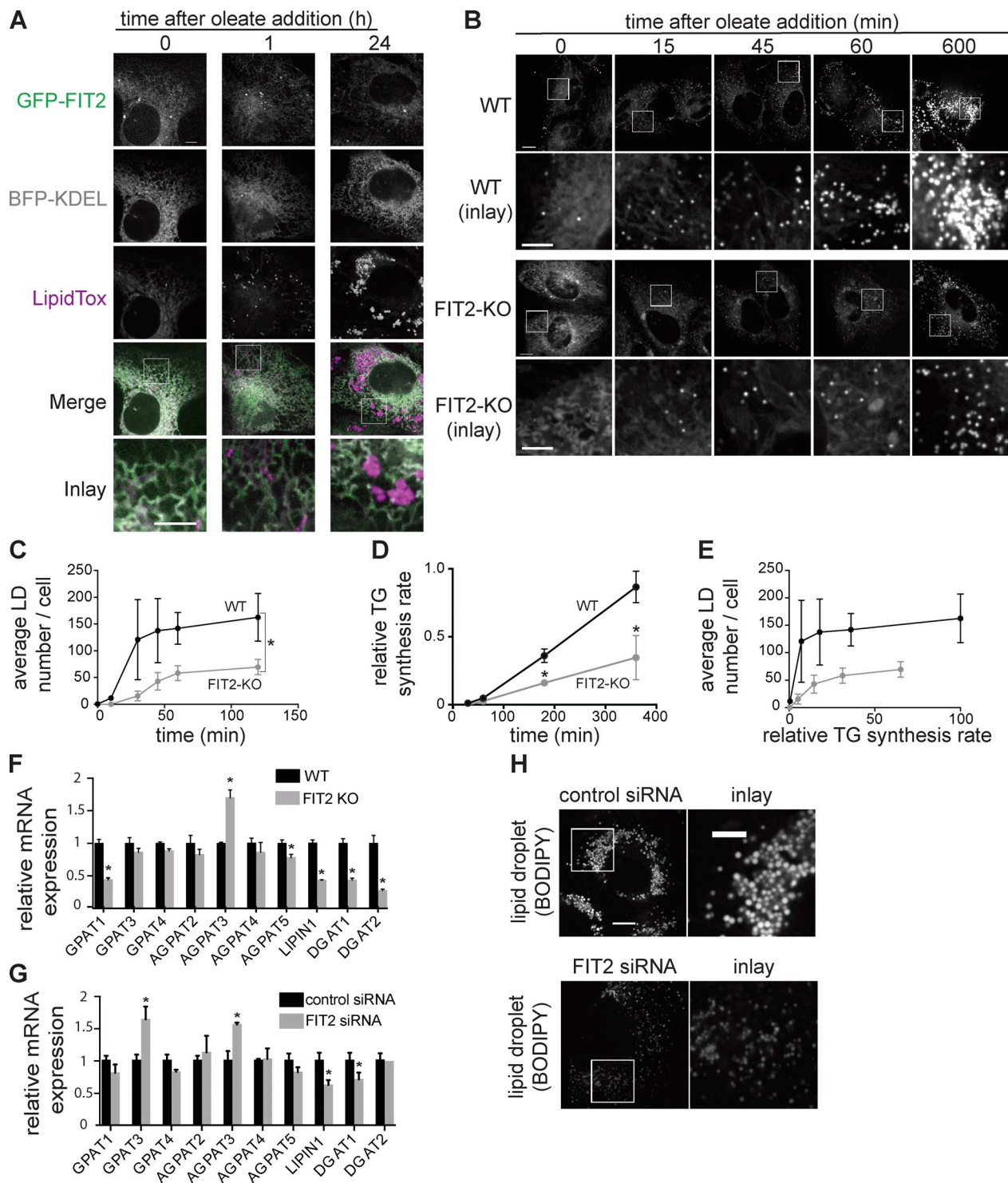


Figure 5. FIT2 is required for normal LD formation. (A) FIT2 localizes diffusely throughout the ER. SUM159 cells expressing endogenous GFP-tagged FIT2 transfected with plasmid expressing the luminal ER marker ssBFP-KDEL were imaged before and after addition of oleic acid at the indicated time. LDs were stained with LipidTOX. Scale bar = 10 μ m. (B) FIT2 deletion results in fewer and smaller LDs formed in response to oleate treatment. Time course of LD formation in FIT2 WT and FIT2-KO SUM159 cells. Cells were treated with 500 μ M oleic acid for the indicated times, and LDs were stained with BODIPY 493/503. Scale bar = 10 μ m. (C) Quantification of LD formation shown in B. $n = 4$ cells. Values represent mean \pm SD (two-way ANOVA; *, $P < 0.001$). (D) Reduced triacylglycerol synthesis in FIT2-KO cells. Cells were pulse-labeled with [14 C]oleate, and incorporation into TG was measured over time by TLC. Mean value of TG band intensity was plotted over time and quantified from three independent measurements \pm SD. Values were calculated relative to WT cells' highest value at 360 min (two-way ANOVA with Sidak test; *, $P < 0.0001$). (E) FIT2-deficient cells form fewer LDs for similar amounts of synthesized TG. Average LD number per cell measured in B was plotted against TG amount calculated in C. (F) Reduced mRNA expression of lipid synthesis enzymes in FIT2-KO cells. mRNA levels of genes involved in the Kennedy pathway in FIT2 WT and FIT2-KO cells were assessed by qPCR analysis. Values represent mean \pm SD relative to WT value; $n = 3$. The figure is representative of three independent experiments (two-way ANOVA with Sidak test; *, $P < 0.01$). (G) Knockdown of FIT2 results in reduced

DGAT1 and LIPIN1 mRNA expression levels. mRNA levels of genes involved in the Kennedy pathway were assessed by qPCR analysis of WT cells pretreated with control or FIT2 siRNA-treated cells. Values represent mean \pm SD relative to WT value; $n = 3$. The figure is representative of two independent experiments (two-way ANOVA with Sidak test; *, $P < 0.05$). **(H)** FIT2 siRNA-treated cells have fewer LDs than control siRNA-treated cells. WT cells were pretreated for 48 h with siRNA targeting FIT2 or control siRNA, and then oleic acid was added for another 48 h before imaging. Scale bar = 5 μ m.

FreeStyle 293 medium (Thermo Fisher Scientific) according to the manufacturer's instructions.

Yeast growth conditions

All yeast strains were derivatives of the BY4741 strain (Table S1). Yeast was transformed by a standard lithium acetate/polyethylene glycol procedure. Cells were grown in synthetic complete (SC) medium containing 2% (wt/vol) glucose without uracil or leucine for plasmid selection. For imaging,

cells transformed with the indicated plasmids were grown in SC-Ura-Leu medium overnight and imaged during early log phase ($A_{600} < 0.3$) the next day. For LD induction, inducible LD strains were precultured to early exponential phase ($A_{600} < 0.3$) in SC medium containing 2% (wt/vol) glucose and then diluted ($A_{600} < 0.05$) in SC medium containing 2% raffinose (wt/vol) overnight. When cultures reached A_{600} of 0.4–0.6, 2% galactose (wt/vol) was added to the raffinose-grown cells to induce LD formation.

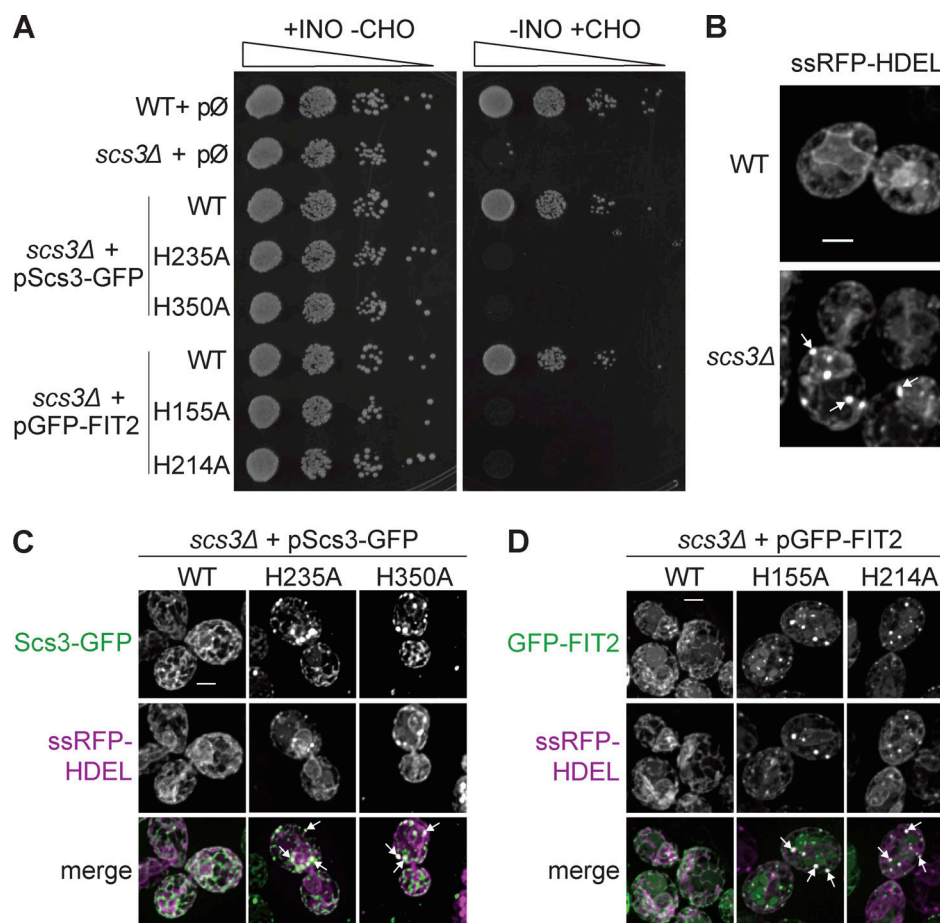


Figure 6. Catalytic residues of FIT2 and Scs3 are required for their Function in vivo in yeast. (A) C2 or C3 histidine mutations of Scs3 or FIT2 did not rescue *scs3Δ* inositol auxotrophy. WT cells, *scs3Δ* cells, and *scs3Δ* cells expressing GFP-tagged Scs3 or FIT2 WT or mutated for C2 histidine to alanine (H235A for Scs3, H155A for FIT2) or C3 histidine to alanine (H350A for Scs3, H214A for FIT2) on a plasmid were serially diluted and spotted on complete solid medium (+INO-CHO) or inositol-depleted (-INO+CHO). To aggravate the growth defect (Villa-García et al., 2011), inositol-depleted medium was supplemented with choline (+CHO), and cells were grown at 37°C. The plates were imaged after 4–5 d. **(B)** SCS3 deletion leads to formation of ER patches. Maximum-intensity projections of representative deconvolved confocal image stacks from WT and *scs3Δ* cells expressing the ER marker ssRFP-HDEL are shown; white arrows highlight ER patches. Scale bar = 2 μ m. **(C)** Reintroduction of Scs3-GFP mutated at C2 or C3 histidine does not restore normal ER shape in *scs3Δ* cells. Subcellular localization of Scs3-GFP WT or H235A and H350A, respectively, were assessed in *scs3Δ* cells. Maximum-intensity projections of representative deconvolved confocal image stacks are presented. Impact on ER shape was addressed with ssRFP-HDEL marker; white arrows highlight ER patches. Scale bar = 2 μ m. **(D)** Reintroduction of GFP-FIT2 mutated at C2 or C3 histidine did not restore normal ER shape in *scs3Δ*. Subcellular localization of GFP-FIT2 WT or H155A and H214A, respectively, were assessed in *scs3Δ* cells. Maximum-intensity projections of representative deconvolved confocal image stacks are presented. Impact on the ER shape was addressed with ssRFP-HDEL marker; white arrows highlight ER patches. Scale bar = 2 μ m.

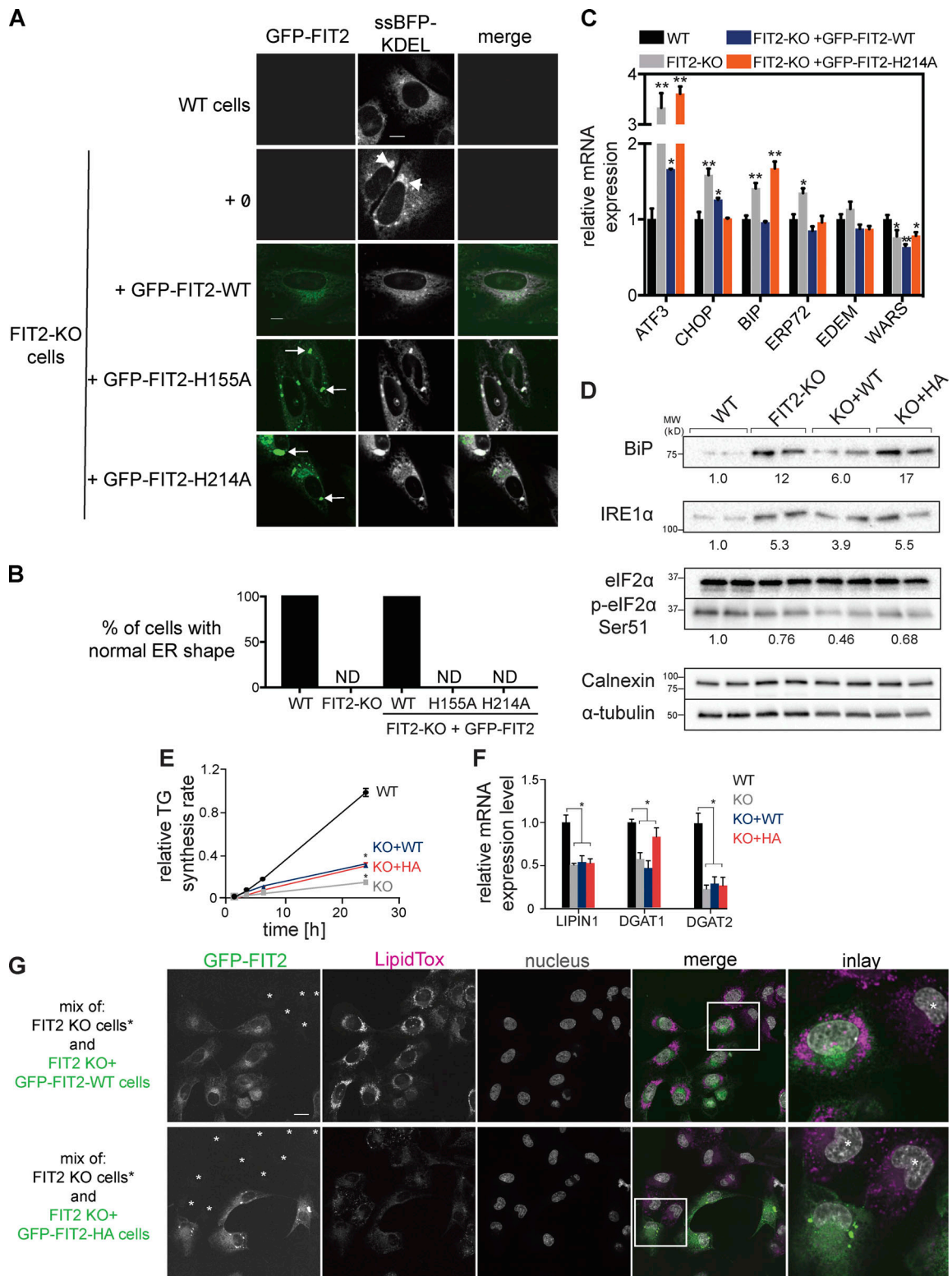


Figure 7. **FIT2 catalytic residues are required for ER homeostasis and normal lipid storage in human cells.** (A and B) Reintroduction of GFP-FIT2 mutated at conserved histidines did not restore normal ER shape in FIT2 KO cells. (A) Representative confocal images of FIT2 WT cells and FIT2-KO cells transiently coexpressing the ER marker ssBFP-KDEL and GFP-FIT2 WT or C2 (H155A) or C3 histidine mutants (H214A). White arrows highlight ER patches. Scale bar = 10 μ m. (B) Quantification of the percentage of rescued ER shape ($n = 50$) is presented under the images. ND, not detected. (C and D) Reintroduction of GFP-FIT2 mutated at H214A did not restore normal ER stress markers expression. (C) qPCR analysis of the indicated genes (values represent mean \pm SD; $n = 3$, representative of three independent experiments; two-way ANOVA with Sidak test; *, $P < 0.01$; **, $P < 0.001$). (D) Western blot analysis of ER stress proteins in FIT2 WT cells, FIT2-KO cells, and FIT2-KO cells stably expressing either WT GFP-FIT2 (KO + WT) or GFP-FIT2-H214A (KO + HA). Quantification of band intensity relative to WT untreated is shown under each panel. (E) Reintroduction of WT GFP-FIT2 or H155A did not restore normal TG synthesis rate in FIT2-KO cells.

FIT2 WT, FIT2-KO cells, and FIT2-KO cells stably expressing either WT GFP-FIT2 (KO+WT) or GFP-FIT2-H214A (KO+HA) were pulse labeled with [¹⁴C]oleate, and incorporation into TG was measured by TLC over time during oleate treatment. Mean value of TG band intensity was plotted over time and quantified from three independent measurements. Values were calculated relative to the value of WT cells at 24 h (two-way ANOVA with Sidak test; *, $P < 0.01$). **(F)** Reintroduction of WT GFP-FIT2 or H214A did not restore normal expression of neutral lipid synthesis genes in FIT2-KO cells. qPCR analysis of the indicated genes was performed on FIT2 WT cells, FIT2-KO cells, and add-back cell lines. Values represent mean \pm SD; $n = 3$. The figure represents three independent experiments (two-way ANOVA with Sidak test; *, $P < 0.01$). **(G)** Reintroduction of WT GFP-FIT2 but not H214A restores LD budding in FIT2-KO cells. FIT2-KO cells were grown together with add-back cell lines expressing GFP-FIT2 WT (top panels) or GFP-FIT2 H214A (bottom panels), and 500 μ M oleic acid was added for 24 h before imaging. LDs were stained with LipidTOX. Nuclei were stained with Hoechst. FIT2-KO cells (labeled with asterisks) were distinguished from add-back cells on the basis of GFP signal. Scale bar = 25 μ m. MW, molecular weight.

Yeast growth assays

WT or *scs3Δ* yeast transformed with the indicated plasmids was grown overnight in SC without uracil liquid culture to stationary phase and spotted in 10-fold serial dilutions onto synthetic medium plates without uracil with or without inositol and with or without choline (2 μ g/ μ l). Images were obtained after 4–5 d of growth at 37°C.

Antibodies and Western blots

Polyclonal antibody against human FIT2 was generated in rabbits (GenScript), affinity purified, and used at a 1:1,000 dilution for Western blot analysis. The peptide sequence of the epitope corresponds to the last 16 aa (PQSCSLNLKQDSYKKP). We used antibodies against FLAG (M2 F3165; MilliporeSigma), tubulin (T5168; MilliporeSigma), calnexin (C5C9; Cell Signaling Technology), GFP (11814460001; Roche), eIF2 α (9722S; Cell Signaling Technology), phospho-eIF2 α (9721S; Cell Signaling Technology), Ire1 α (3294; Cell Signaling Technology), and BiP (3177; Cell Signaling Technology). Crude extract samples for Western blot analysis were prepared as described previously (Wang et al., 2016). Briefly, cells were lysed with lysis buffer (150 mM NaCl, 50 mM Tris-HCl, pH 7.4, 1% Triton X-100) and spun for 6 min at 16,000 *g*. The supernatant was denatured in Laemmli buffer at 37°C for 10 min. Proteins were separated on a 4–15% SDS-PAGE gel (Bio-Rad Laboratories) and transferred to a polyvinylidene difluoride membrane (Bio-Rad Laboratories).

RNA extraction and real-time qPCR

Total RNA was isolated using the RNeasy Kit (Qiagen) according to the manufacturer's instructions. cDNA was synthesized using the iScript cDNA synthesis kit (Bio-Rad Laboratories), and qPCR was performed in triplicates using the Power SYBR Green PCR Master Mix Kit (Applied Biosystems). Sequences of the qPCR primers used are listed in Table S2.

Plasmid constructs

Plasmids in this paper are described in Table S3. To obtain alcohol dehydrogenase promoter (pADH):*Scs3*-GFP (pMB86) and pADH:GFP-*Scs3* (pMB87), the *SCS3* gene was amplified from BY4741 gDNA, inserted into pCRII-ZeroBlunt (Life Technologies; pMB88), and subcloned into XbaI-EcoRI sites of pRS416 (pMB98) to make pMB86 and into XhoI-EcoRI sites of pRS416 (pMB99) to make pMB87. Site-directed mutagenesis (QuikChange Lightning Site-Directed Mutagenesis Kit; Agilent) was performed by PCR using mutagenic oligonucleotides with pMB88 as the template. Mutagenized plasmids were checked by sequencing, and a region containing the mutation was systematically subcloned into the

original pMB98 using endogenous restriction sites to prevent mutations that may have occurred elsewhere on the plasmid. Mutations on pMB86 of the C2 and C3 conserved histidines to alanines led to pMB96 and pMB97, respectively. The pADH:FIT2-GFP (pMB104) and pADH:GFP-FIT2 (pMB111) were amplified from human FIT2 cDNA NM_001080472.2 (OriGene) and subcloned into the XbaI-EcoRI sites of pRS416 (pMB98) to make pMB104 and into XhoI-EcoRI sites of pRS416 (pMB99) to make pMB111. Mutation on pMB111 of the C2 and C3 conserved histidines to alanines led to pMB112 and pMB113, respectively. Plasmids used for safe harbor integration were derived from the AAVS1-PGK1 Homologous Recombination donor plasmid (Addgene; 68375). WT GFP-FIT2 and H155A sequences were cloned using XbaI/KpnI restriction sites. The same plasmids were also used for transient transfection of SUM159 cells. Plasmids used for protein purification as well as for FIT2 overexpression in human GnTI-293 cells were derived from the plasmid cytomegalovirus (pCMV) 14 backbone. FIT2 WT or H155A/H214A sequences were cloned in EcoRI/BamHI sites to obtain pCMV-FIT2-3FLAG WT (pMB82) and H155A/H214A (pMB277).

Generating cell line KO and knock-in in SUM159 cells

To generate CRISPR FIT2-KO SUM159 cell lines, we used a lentiviral delivery method as previously described (Sanjana et al., 2014). The sequence 5'-CGGGGTGCACTCACACGTTG-3' was used as a gRNA to direct Cas9 to exon 1 of the FIT2 locus. The gRNA was cloned into the LentiCRISPR V2 plasmid (Addgene; 52961). Briefly, the LentiCRISPR V2, psPAX2 (Addgene; 12260), and pCMV-VSVG (Addgene; 8454) plasmids were transfected into HEK293 packaging cells, and lentiviral particles were collected from the culture media 24 h later and used to infect SUM159 cells. One day after infection, cells were treated with puromycin for 3 d to select for infected cells. Cells were replated onto 150-mm dishes at clonal density. Individual colonies were isolated in 24-well dishes. Screening of clones was performed by qPCR (sense primer 5'-GTACATCTGCACCTCCATCTTC-3'; antisense primer 5'-CTTGCTCTGGTGTTCCTTTCTG-3') using Power SYBR Green (Life Technologies). gDNA of clones showing mRNA expression defects was extracted (Epicentre QuickExtract DNA Extraction Solution; Lucigen), and the genomic sequence surrounding the target exon of FIT2 was amplified by PCR (sense 5'-TCAAGCTGTGGGACTCGCGG-3' and antisense 5'-TCCAATGACTCGTCCACCAC-3'). PCR products were subcloned into a plasmid (Zero Blunt TOPO PCR Cloning Kit; Life Technologies) to validate the edited region of positive KO clones by sequencing. The KO was also confirmed

by Western blot analysis using a custom-made anti-FIT2 antibody.

To generate cell lines stably expressing GFP-FIT2 in FIT2-KO SUM159 cells, we used the AAVS1 safe harbor targeting method (System Biosciences). WT GFP-FIT2 or H155A donor constructs were cotransfected with a hCas9 plasmid and a gRNA-AAVS1-T2 plasmid using Lipofectamine 3000 (Thermo Fisher Scientific) according to the manufacturer's instructions. Cells were selected with puromycin for 3 d, and single-cell FACS sorting was performed on the basis of GFP signal. Positive clones were confirmed by fluorescence microscopy and by Western blotting with anti-FIT2 antibody.

To generate a GFP-FIT2 knock-in SUM159 cell line, the sequence 5'-GTGGCTGACGAGATCCGGCA-3' was used as a gRNA to direct Cas9 to exon 1 of the FIT2 locus. The gRNA was cloned into the pX459 plasmid (Addgene; 62988). The GFP-FIT2 donor template (pMB264) was generated and cotransfected with pX459 in SUM159 cells using FuGENE (Promega) according to the manufacturer's instructions. Cells were selected with puromycin for 3 d, and single-cell FACS sorting was performed on the basis of GFP signal. Positive clones were confirmed by fluorescence microscopy and by Western blotting with anti-FIT2 antibody.

Oleoyl CoA flux measurement in microsomes

Human Expi293F GnTI⁻ suspension cells were transfected with plasmids pMB82 (FIT2 WT-3FLAG) or pMB277 (FIT2 HHAA-3FLAG) with 1 mg/ml poly(ethyleneimine; MilliporeSigma). 10 mM sodium butyrate (MilliporeSigma) was added to the cell culture 16 h after transfection, and cells were harvested after 48 h. The cell pellet was resuspended in lysis buffer (250 mM sucrose, 50 mM Tris-HCl, pH 7.4, 200 mM NaCl, 1 mM EDTA) plus protease inhibitors (Roche) and lysed with Dounce homogenizer. The cell lysate was centrifuged at 8,000 *g* for 10 min at 4°C to remove cell debris, and the supernatant was further centrifuged at 100,000 *g* for 60 min at 4°C. The membrane pellet was gently resuspended in lysis buffer. 100 µg of microsomes were mixed with reaction buffer (100 mM KAc, pH 7, 1 mM MgCl₂, 20 mM NaCl, 0.625 mg/ml BSA) and lysis buffer to a final volume of 200 µl. The assay was started by adding 25 µM oleoyl-CoA containing [¹⁴C]oleoyl-CoA (American Radiolabeled Chemicals) as a tracer (0.1 µCi) and incubated at 37°C. The reaction was stopped by adding chloroform/methanol (2:1) and 2% phosphoric acid. The lower phase was extracted, dried under an air stream, resuspended in chloroform, and separated by TLC with a chloroform/methanol/water (65:25:4) or chloroform/methanol (24:1) solvent system to separate polar and neutral lipids, respectively. The TLC plates were exposed overnight to a phosphor imager screen and developed with the Typhoon FLA 7000 phosphor imager.

Recombinant FIT2 protein purification

Human Expi293F GnTI⁻ cells were used to produce 3FLAG-tagged human FIT2 protein by following the same expression protocol as the microsomal assay. The cell pellet was lysed with a Branson sonicator with lysis buffer (50 mM Tris-HCl, pH 7.4, 200 mM NaCl) plus protease inhibitors (Roche). The lysate was

centrifuged for 15 min at 10,000 *g* to remove cell debris. The supernatant was then centrifuged for 60 min at 100,000 *g*. The membrane fraction (pellet) was resuspended in lysis buffer supplemented with 1% glyco-diosgenin (GDN; Anatrace) and incubated overnight at 4°C. Unsolubilized membranes were removed by ultracentrifugation at 100,000 *g* for 60 min. The supernatant fraction containing solubilized FIT2 was incubated with anti-FLAG M2 Affinity Gel (MilliporeSigma) for 3 h, and the sample was transferred to 25-ml BioSpin columns and washed by gravity flow with lysis buffer supplemented with 0.1% GDN. Proteins were eluted for 5-min sequential elutions (performed five times) in 500 µl of lysis buffer containing 0.1% GDN and 0.2 µg/µl poly-FLAG peptide (bimake.com). Eluted fractions were pooled and concentrated using 10 kD Amicon Ultra-4 Centrifugal Filter Units (MilliporeSigma). Protein concentrations were calculated by comparing band intensity of 2 µl of eluate with a BSA standard on a 4–15% SDS-PAGE gels (Bio-Rad Laboratories) and visualized by using Coomassie blue (Imperial Protein Stain; Thermo Fisher Scientific). Aliquots were stored in elution buffer supplementing with 10% glycerol at 80°C.

Enzymatic assays

Oleoyl-CoA diphosphatase activity was measured by following the formation of [¹⁴C]oleoyl 4'-phosphopantetheine by TLC from [¹⁴C]oleoyl-CoA (American Radiolabeled Chemicals). For time-dependent reactions, the reaction mixture comprised 5 µM of oleoyl-CoA containing traces of [¹⁴C]oleoyl-CoA (0.005 µCi) in reaction buffer with 50 mM Tris-HCl (pH 7.5), 200 mM NaCl, 0.5 mM MgCl₂, and 0.1% GDN. 25 ng of enzyme protein were added in a total volume of 0.2 ml of reaction mixture and incubated at 37°C for the indicated time. For substrate-dependent reactions, serial dilution of 2 mM oleoyl-CoA containing traces of [¹⁴C]oleoyl-CoA (0.01 µCi/µl) was made and incubated with 25 ng of enzyme proteins for 10 min at 37°C. The reaction was stopped by adding a chloroform/methanol mixture (2:1) and phosphoric acid 2%. After centrifugation for 5 min at 5,000 *g*, the lower phase was extracted, dried under an air stream, resuspended in chloroform, and separated by TLC using a chloroform/methanol/water (65:25:4) solvent system. The TLC plate was exposed to a phosphor imaging screen overnight and was revealed with the Typhoon FLA 7000 phosphor imager. The band intensity was quantified using ImageJ software. Enzyme assays were conducted in triplicate in two independent experiments.

For competition assays, 25 ng of recombinant FIT2 WT protein was incubated for 10 min at 37°C with 5 µM of oleoyl-CoA containing traces of [¹⁴C]oleoyl-CoA (0.005 µCi) and 25 µM or 50 µM of the indicated unlabeled CoA competitor. The same procedure as described above was used to extract and analyze lipids.

[¹⁴C]Oleic acid labeling of lipids, lipid extraction, and TLC

Cells were pulse labeled with [¹⁴C]oleic acid (50 µCi/µmol), then washed three times with PBS. Lipids were extracted from six-well cell culture plates by adding hexane/isopropanol (3:2) and gently shaking for 10 min. The process was repeated a second

time for full extraction of all lipids. Lipids were dried under a nitrogen stream and separated by TLC using a hexane/diethyl ether/acetic acid (80:20:1) solvent system for neutral lipid separation and a chloroform/methanol/acetone/acetic acid/water (50:10:20:15:5) solvent system for phospholipid separation. TLC plates were exposed to a phosphor imaging screen overnight and analyzed by using a Typhoon FLA 7000 phosphor imager. Incorporation of radiolabeled oleic acid in lipids was determined over time by measuring band intensity by TLC using ImageJ software.

Lipidomics

For the analysis of microsome samples, lipids were extracted using a modified version of the Bligh-Dyer method (Bligh and Dyer, 1959). Briefly, samples were manually shaken in a glass vial (VWR) with 1 ml of PBS, 1 ml of methanol, and 2 ml of chloroform for 30 s. The resulting mixture was vortexed for 15 s and centrifuged at 2,400 *g* for 6 min to induce phase separation. The organic (bottom) layer was retrieved using a Pasteur pipette, dried under a stream of nitrogen, and reconstituted in 2:1 chloroform/methanol for analysis by liquid chromatography-MS. Lipidomic analyses were performed by using the Vanquish HPLC system coupled online to a Q Exactive quadrupole-Orbitrap mass spectrometer equipped with an electrospray ion source (Thermo Fisher Scientific). Data were acquired in positive and negative ionization modes. Solvent A consisted of 95:5 water/methanol, and solvent B was 60:35:5 isopropanol/methanol/water. For positive mode, solvents A and B contained 5 mM ammonium formate with 0.1% formic acid; for negative mode, solvents contained 0.028% ammonium hydroxide. A Bio-Bond (Dikma Technologies) C4 column (5 μ m, 4.6 mm \times 50 mm) was used. The gradient was held at 0% B between 0 and 5 min, raised to 20% B at 5.1 min, increased linearly from 20% to 100% B between 5.1 and 55 min, held at 100% B between 55 min and 63 min, returned to 0% B at 63.1 min, and held at 0% B until 70 min. The flow rates were 0.1 ml/min from 0 to 5 min, 0.4 ml/min between 5.1 min and 55 min, and 0.5 ml/min between 55 min and 70 min. Spray voltages were 3.5 kV and 2.5 kV for positive and negative ionization modes, respectively. Sheath, auxiliary, and sweep gases were 53, 14, and 3, respectively. The capillary temperature was 275°C. Data were collected in full MS/dd-MS2 mode (top 5). Full MS scans were acquired from 100–1,500 mass-to-charge ratio (*m/z*) with a resolution of 70,000, automatic gain control (AGC) target of $1e^6$, and a maximum injection time of 100 ms. MS2 scans were acquired with a resolution of 17,500, a fixed first mass of 50 *m/z*, AGC target of $1e^5$, and a maximum injection time of 200 ms. Stepped normalized collision energies were 20%, 30%, and 40%. Data alignment, peak integration, and comparison between sample conditions were performed with Dilu (github.com/bathyg/dilu). Mass accuracy and chromatography checks and peak integration of all Dilu-identified lipids were performed with Skyline (MacLean et al., 2010).

To identify oleoyl 4'-phosphopantetheine as an FIT2 product, 50 μ M oleoyl-CoA was incubated for 30 min with 500 ng of recombinant FIT2 WT or FIT2 HHAA. Lipid extraction and TLC were performed as described. The silica plate was scraped at

the known migration location of lipid 1. Lipids were extracted with 5 ml of chloroform/methanol 2:1 for 2 h in the cold room. 2 ml of 2% phosphoric acid was added for 15 min. After centrifugation at low speed, the lower phase was recovered, dried under a nitrogen stream and resuspended in methanol. The analyte was directly infused into the Q-Exactive-Orbitrap mass spectrometer (Thermo Fisher Scientific) at a flow rate of 10 μ l/min and the spray voltage was set to 3 kV. The heated capillary and the heated electrospray ionization were held at 320°C and 300°C, respectively. Fourier transform MS spectra were acquired in positive ion mode at resolution *m/z* = 70,000 in the Orbitrap analyzer. For tandem MS spectra, the precursor ion with *m/z* = 623.3 was isolated with a window of 1 D and fragmented at a normalized higher collision energy of 15 units.

Cellular acyl-CoA esters were analyzed using a method based on a previously published report (Magnes et al., 2005) that relies on the extraction procedure described by Deutsch et al. (1994). The CoAs were further purified by solid-phase extraction as described by Minkler et al. (2008). The acyl-CoAs were analyzed by flow injection analysis using positive electrospray ionization on a Xevo TQ-S triple quadrupole mass spectrometer (Waters) using methanol/water (80:20 vol/vol) containing 30 mM ammonium hydroxide as the mobile phase. Spectra were acquired in the multichannel acquisition mode, monitoring the neutral loss of 507,003 D (phosphor-ADP) and scanning from *m/z* 750 to 1,060. Heptadecanoyl CoA was employed as an internal standard. The endogenous CoAs were quantified using calibrators prepared by spiking cell or liver homogenates with authentic CoAs (MilliporeSigma) having saturated acyl chain lengths C0–C18. Corrections for the heavy isotope effects, mainly ^{13}C , to the adjacent *m* + 2 spectral peaks in a particular chain length cluster were made empirically by referring to the observed spectra for the analytical standards.

Live-cell imaging and image processing

Microscopy was performed on a spinning disk confocal microscope (Yokogawa CSU-X1) set up on a Nikon Eclipse Ti inverted microscope with a 100 Apochromat total internal reflection fluorescence/1.4 NA objective (Nikon) in line with 2 \times amplification. Fluorophores were excited with 405-, 488-, or 561-nm laser lines, and fluorescence was detected by an iXon Ultra 897 EMCCD camera (Andor) or a Zyla 4.2 Plus scientific complementary metal-oxide-semiconductor camera (Andor). Bandpass filters (Chroma Technology) were applied to all acquisitions. When applicable, maximum-intensity Z stacks of 0.15-mm slices were obtained with piezo Z-stage. For live-cell imaging, temperature, humidity, and CO₂ were controlled during imaging using a stage-top chamber (OKOLAB).

For imaging of initial LD formation or late events, 500 μ M oleic acid (MilliporeSigma) complexed with 0.5% fatty acid-free BSA (MilliporeSigma) was added to wells immediately before image acquisition. When applicable, 0.5 mg/ml BODIPY 493/503 (Life Technologies) or HCS LipidTOX Deep Red Neutral Lipid Stain (Thermo Fisher Scientific) was added before and with oleic acid supplementation to stain LDs.

Acquired images were processed and quantified manually with Fiji software (<http://fiji.sc/Fiji>). The plugin “Find Maxima” was used to quantify the LD number. In yeast, CellProfiler software (<https://cellprofiler.org/>) was used to quantify LD numbers in SUM159 cells using an automated pipeline. All quantifications were performed on raw images. Deconvolution of images in Fig. 6 was performed using Huygens Professional 15.05 (Scientific Volume Imaging) with classic maximum likelihood estimation algorithm using a calculated point spread function for each wavelength.

Quantification of ER sheets and tubules

0.25- μm maximum-intensity Z stack images were acquired on a confocal spinning-disk microscope from cells expressing the ER marker $\alpha\text{GFP-KDEL}$. From these images, sheets and tubules were quantified from masks obtained via supervised segmentation. The pipeline had the following seven steps: (1) A few volume crops were annotated, with a subset of their voxels being labeled as background, tubules, or sheets. (2) A machine learning (random forest) model (<https://github.com/HMS-IDAC/VoxelClassifier>) was trained to classify voxels on the basis of provided annotations. (3) A dataset of cropped regions to be analyzed was generated. (Because voxel classification in 3D is computationally time-consuming, this step speeds up analysis considerably.) (4) The trained machine learning model was applied on cropped regions from step 3 to generate masks with segmented sheet/tubule areas. (5) An algorithm based on Watershed (Roesdink and Meijster, 2000) and Active Contours (Chan and Vese, 2001) was deployed on the cropped regions and the corresponding probability maps to create nuclei and cell masks. (6) Layer masks of ~ 25 -voxel thickness were generated outwardly from the nucleus using morphological dilation, and the number of sheets and tubules in such masks was computed up to 20 layers or until the amount of sheet voxels stopped growing, whichever happened first. (7) Step 6 was repeated after the cropped regions and probability maps were resized so that the cell mask volume was equal to the average cell volume in the analyzed dataset.

Immunofluorescence

For standard immunofluorescence experiments, cells were grown on glass-bottomed six-well plates and fixed with 4% formaldehyde. Blocking was performed with 3% BSA in PBS with 0.1% Triton X-100. Primary and secondary antibody dilutions were performed in the same solution. We used anti-protein disulfide isomerase (2792; Abcam) to detect ER, anti-LC3 (2775S; Cell Signaling Technology) to detect autophagy, anti-LAMP1 (D2D11; Cell Signaling Technology) to detect lysosomes, anticatalase (D4P7B; Cell Signaling Technology) to detect peroxisomes, and anti-GM130 (D6B1; Cell Signaling Technology) to detect the Golgi apparatus. We used as a secondary antibody Alexa Fluor 568-conjugated secondary antibodies (Life Technologies). Nuclei were stained with 1 $\mu\text{g}/\text{ml}$ Hoechst 33342 (Life Technologies) during one of the post-secondary antibody washes.

EM

Cells in Petri dishes were fixed in 2.5% glutaraldehyde in 0.1 M sodium cacodylate buffer, pH 7.4, for 1 h. Buffer-rinsed cells were scraped in 1% gelatin and spun down in 2% agar. Chilled

blocks were trimmed and postfixed in 1% osmium tetroxide for 1 h. The samples were rinsed three times in sodium cacodylate buffer and postfixed in 1% osmium tetroxide for 1 h. Samples were then rinsed and stained en bloc in aqueous 2% uranyl acetate for 1 h, followed by rinsing, dehydrating in an ethanol series, and infiltrating with Embed 812 (Electron Microscopy Sciences) resin, and then they were baked overnight at 60°C. Hardened blocks were cut using a Leica UltraCut UC7. Sections (60 nm) were collected on formvar/carbon-coated nickel grids and contrast stained with 2% uranyl acetate and lead citrate. They were viewed using an FEI Tencai Biotwin transmission electron microscope at 80 kV. Images were obtained on a Morada charge-coupled device using iTEM software (Olympus).

Lattice light-sheet microscopy

Imaging was performed on a lattice light-sheet microscope developed by Chen et al. (2014). SUM159 cells were transfected with the ER marker αGFP (Addgene; 68069) and imaged at 37°C in Leibovitz’s L-15 medium (Thermo Fisher Scientific; 11415064) supplemented with 5% heat-inactivated FBS (GE Healthcare Life Sciences; SH30071.03), 100 U/ml penicillin and 100 $\mu\text{g}/\text{ml}$ streptomycin (Thermo Fisher Scientific; 15140122), 1 $\mu\text{g}/\text{ml}$ hydrocortisone (MilliporeSigma; H0888), 25 mM Hepes (Thermo Fisher Scientific; 15630080), and 5 $\mu\text{g}/\text{ml}$ insulin (Cell Applications; 128). A square lattice light sheet was generated and passed through an annular mask with inner and outer NAs of 0.42 and 0.50, respectively. The beam was dithered through the sample during acquisition. Cell volumes were acquired by stepping the sample stage at 400-nm intervals between 221 and 251 times with a 35-ms exposure for each plane. Cells were excited with a 488-nm laser (~ 300 -mW power; ~ 15.87 μW – 28.9 μW measured at the back aperture of the excitation objective during experiments). Fluorescence was detected with a 25 \times /1.1 NA Nikon CFI Plan Apochromat long working-distance objective, passed through a 488-nm StopLine single-notch filter (Semrock; NF03-488E-25), a 446/523/600/677-nm Brightline quad-band band-pass filter (Semrock; FF01-446/523/600/677-25), and a custom dichroic transmitting 390–555 nm, 645–875 nm, and reflecting 565–630 nm onto a Hamamatsu ORCA Flash 4.0 scientific complementary metal-oxide-semiconductor camera. Images were captured as 1,024 \times 256-pixel planes and subsequently deskewed and background corrected using SlideBook software. Imaging data were loaded into MATLAB using code (Aguet et al., 2016) and subsequently deconvolved by providing measured background and an experimentally measured point spread function for 15 iterations using a Richardson-Lucy algorithm adapted to run on a graphics processing unit.

Statistical analysis

All results were analyzed using Prism software (GraphPad Software) and the tests specified in the figure legends, unless otherwise stated. All error bars represent the SD.

Online supplemental material

Fig. S1 shows FIT2 homology with LPP enzymes and characterization of FIT2 activity. Fig. S2 depicts characterization of FIT2-KO SUM159 clones. Fig. S3 shows the impact of FIT2 deletion on

other organelles. Fig. S4 illustrates FIT2-KD efficiency, ER feature quantification, and characterization of the cell line expressing endogenously GFP-tagged FIT2. Fig. S5 shows the results of yeast assays of FIT2 and SCS3 function. Table S1 lists yeast strains used. Table S2 lists qPCR primers used. Table S3 lists plasmids used.

Acknowledgments

We thank members of the laboratory for technical assistance and helpful comments on the manuscript; David Silver (Duke-NUS Medical School, Singapore) and Sebastien Léon (Institut Jacques Monod, Paris, France) for reagents; Tom Rapoport (Harvard University, Boston, MA), Tim Levine (University College London, London, England), Christian Dibble (Beth Israel Deaconess Medical Center, Boston, MA) and Brenda Schulman (Max Planck Institute of Biochemistry, Munich, Germany) for helpful discussions; and Gary Howard for editorial assistance.

M. Becuwe is a recipient of a fellowship from the Jane Coffin Childs Memorial Fund for Medical Research. L.M. Bond was supported by National Institutes of Health grant T32DK007477. N. Mejhert is a recipient of a fellowship from Marie Skłodowska-Curie actions. This work was supported by the Mass Spectrometry Core of the Salk Institute for Biological Studies with funding from a National Cancer Institute cancer center support grant (P30 014195), the Helmsley Center for Genomic Medicine, and the National Institutes of Health (grant 1S10OD021815-01) and by National Institutes of Health grants R01DK106210 (to A. Saghatelian), 5R01GM124348 (to R.V. Farese), and R01GM097194 (to T.C. Walther). T.C. Walther is a Howard Hughes Medical Institute investigator.

The authors declare no competing financial interests.

Author contributions: M. Becuwe, T.C. Walther, and R.V. Farese Jr. conceived the project. M. Becuwe acquired and analyzed the data. N. Mejhert performed the image analysis of LD formation. S.D. Elliott helped to establish the stable cell lines and did the lattice light sheet microscopy acquisition. S. Boland performed the direct infusion experiment and analyzed the data. L.M. Bond helped in the enzymatic activities and protein purification and did the qPCR analysis. M. Cicconet did the endoplasmic reticulum features quantification. X.N. Liu and M.M. Graham performed the EM. O. Ilkayeva measured acyl-CoA levels in cells by mass spectrometry. A.F.M. Pinto and A. Saghatelian performed mass spectrometry analyses on microsomes to identify FIT2 products. All authors discussed the results. M. Becuwe, T.C. Walther, and R.V. Farese Jr. wrote the paper.

Submitted: 17 June 2020

Revised: 16 July 2020

Accepted: 17 July 2020

References

Aguet, F., S. Upadhyayula, R. Gaudin, Y.-Y. Chou, E. Cocucci, K. He, B.-C. Chen, K. Mosaliganti, M. Pasham, W. Skillern, et al. 2016. Membrane dynamics of dividing cells imaged by lattice light-sheet microscopy. *Mol. Biol. Cell*. 27:3418–3435. <https://doi.org/10.1091/mbc.e16-03-0164>

Becuwe, M., L.M. Bond, N. Mejhert, S. Boland, S.D. Elliott, M. Cicconet, X.N. Liu, M.M. Graham, T.C. Walther, and R.V. Farese Jr. 2018. FIT2 is a lipid

phosphate phosphatase crucial for endoplasmic reticulum homeostasis. *bioRxiv*. doi: (Preprint posted March 29, 2018) <https://doi.org/10.1101/291765>

Bligh, E.G., and W.J. Dyer. 1959. A rapid method of total lipid extraction and purification. *Can J Biochem Physiol*. 37(8):911–917. <https://doi.org/10.1139/o59-099>

Cartwright, B.R., D.D. Binns, C.L. Hilton, S. Han, Q. Gao, and J.M. Goodman. 2015. Seipin performs dissectible functions in promoting lipid droplet biogenesis and regulating droplet morphology. *Mol. Biol. Cell*. 26:726–739.

Chan, T.F., and L.A. Vese. 2001. Active contours without edges. *IEEE Trans. Image Process*. 10:266–277. <https://doi.org/10.1109/83.902291>

Chang, T.-Y., B.-L. Li, C.C.Y. Chang, and Y. Urano. 2009. Acyl-coenzyme A: cholesterol acyltransferases. *Am. J. Physiol. Endocrinol. Metab*. 297:E1–E9. <https://doi.org/10.1152/ajpendo.90926.2008>

Chen, B.C., W.R. Legant, K. Wang, L. Shao, D.E. Milkie, M.W. Davidson, C. Janetopoulos, X.S. Wu, J.A. Hammer, III, Z. Liu, et al. 2014. Lattice light-sheet microscopy: imaging molecules to embryos at high spatiotemporal resolution. *Science*. 346. 1257998. <https://doi.org/10.1126/science.1257998>

Chitraju, C., N. Mejhert, J.T. Haas, L.G. Diaz-Ramirez, C.A. Grueter, J.E. Imbriglio, S. Pinto, S.K. Koliwad, T.C. Walther, and R.V. Farese, Jr. 2017. Triglyceride synthesis by DGAT1 protects adipocytes from lipid-induced ER stress during lipolysis. *Cell Metab*. 26:407–418.e3. <https://doi.org/10.1016/j.cmet.2017.07.012>

Choudhary, V., N. Ojha, A. Golden, and W.A. Prinz. 2015. A conserved family of proteins facilitates nascent lipid droplet budding from the ER. *J. Cell Biol*. 211:261–271. <https://doi.org/10.1083/jcb.201505067>

Choudhary, V., G. Golani, A.S. Joshi, S. Cottier, R. Schneiter, W.A. Prinz, and M.M. Kozlov. 2018. Architecture of lipid droplets in endoplasmic reticulum is determined by phospholipid intrinsic curvature. *Curr. Biol*. 28:915–926.e9. <https://doi.org/10.1016/j.cub.2018.02.020>

Dahlqvist, A., U. Stahl, M. Lenman, A. Banas, M. Lee, L. Sandager, H. Ronne, and S. Stymne. 2000. Phospholipid:diacylglycerol acyltransferase: an enzyme that catalyzes the acyl-CoA-independent formation of triacylglycerol in yeast and plants. *Proc. Natl. Acad. Sci. USA*. 97:6487–692.

Deutsch, J., E. Grange, S.I. Rapoport, and A.D. Purdon. 1994. Isolation and quantitation of long-chain acyl-coenzyme A esters in brain tissue by solid-phase extraction. *Anal. Biochem*. 220:321–323. <https://doi.org/10.1006/abio.1994.1344>

Di Meo, I., C. Colombelli, B. Srinivasan, M. Villiers, J. Hamada, S.Y. Jeong, R. Fox, R.L. Woltjer, P.G. Tepper, L.L. Lahaye, et al. 2017. Acetyl-4'-phosphopantetheine is stable in serum and prevents phenotypes induced by pantothenate kinase deficiency. *Sci. Rep*. 7:11260. <https://doi.org/10.1038/s41598-017-11564-8>

Gasmi, L., and A.G. McLennan. 2001. The mouse *Nudt7* gene encodes a peroxisomal nudix hydrolase specific for coenzyme A and its derivatives. *Biochem. J*. 357:33–38. <https://doi.org/10.1042/bj3570033>

Goh, V.J., J.S.Y. Tan, B.C. Tan, C. Seow, W.-Y. Ong, Y.C. Lim, L. Sun, S. Ghosh, and D.L. Silver. 2015. Postnatal deletion of fat storage-inducing transmembrane protein 2 (FIT2/FITM2) causes lethal enteropathy. *J. Biol. Chem*. 290:25686–25699. <https://doi.org/10.1074/jbc.M115.676700>

Goldstein, J.L., R.A. DeBose-Boyd, and M.S. Brown. 2006. Protein sensors for membrane sterols. *Cell*. 124:35–46. <https://doi.org/10.1016/j.cell.2005.12.022>

Gooding, J.M., M. Shayeghi, and E.D. Saggerson. 2004. Membrane transport of fatty acylcarnitine and free L-carnitine by rat liver microsomes. *Eur. J. Biochem*. 271:954–961. <https://doi.org/10.1111/j.1432-1033.2004.03997.x>

Grevengoed, T.J., E.L. Klett, and R.A. Coleman. 2014. Acyl-CoA metabolism and partitioning. *Annu. Rev. Nutr*. 34:1–30. <https://doi.org/10.1146/annurev-nutr-071813-105541>

Gross, D.A., E.L. Snapp, and D.L. Silver. 2010. Structural insights into triglyceride storage mediated by fat storage-inducing transmembrane (FIT) protein 2. *PLoS One*. 5. e10796. <https://doi.org/10.1371/journal.pone.0010796>

Gross, D.A., C. Zhan, and D.L. Silver. 2011. Direct binding of triglyceride to fat storage-inducing transmembrane proteins 1 and 2 is important for lipid droplet formation. *Proc. Natl. Acad. Sci. USA*. 108:19581–19586. <https://doi.org/10.1073/pnas.1110817108>

Hayes, M., V. Choudhary, N. Ojha, J.J. Shin, G.-S. Han, G.M. Carman, C.J. Loewen, W.A. Prinz, and T. Levine. 2018. Fat storage-inducing transmembrane (FIT or FITM) proteins are related to lipid phosphatase/phosphotransferase enzymes. *Microb. Cell*. 5:88–103. <https://doi.org/10.15698/mic2018.02.614>

Hosaka, K., J. Nikawa, T. Kodaki, H. Ishizu, and S. Yamashita. 1994. Cloning and sequence of the *SCS3* gene which is required for inositol prototrophy in *Saccharomyces cerevisiae*. *J. Biochem*. 116:1317–1321.

- Kadereit, B., P. Kumar, W.-J. Wang, D. Miranda, E.L. Snapp, N. Severina, I. Torregroza, T. Evans, and D.L. Silver. 2008. Evolutionarily conserved gene family important for fat storage. *Proc. Natl. Acad. Sci. USA*. 105: 94–99. <https://doi.org/10.1073/pnas.0708579105>
- Kerr, E.W., S.A. Shumar, and R. Leonardi. 2019. Nudt8 is a novel CoA diphosphohydrolase that resides in the mitochondria. *FEBS Lett.* 593: 1133–1143. <https://doi.org/10.1002/1873-3468.13392>
- MacLean, Brendan, Daniela M Tomazela, Nicholas Shulman, Matthew Chambers, Gregory L Finney, Barbara Frewen, Randall Kern, David L Tabb, Daniel C Liebler, and Michael J MacCoss. 2010. Skyline: an open source document editor for creating and analyzing targeted proteomics experiments. *Bioinformatics*. 26(7):966–968. <https://doi.org/10.1093/bioinformatics/btq054>
- Magnes, C., F.M. Sinner, W. Regittnig, and T.R. Pieber. 2005. LC/MS/MS method for quantitative determination of long-chain fatty acyl-CoAs. *Anal. Chem.* 77:2889–2894. <https://doi.org/10.1021/ac048314i>
- McLennan, A.G. 2006. The Nudix hydrolase superfamily. *Cell. Mol. Life Sci.* 63:123–143. <https://doi.org/10.1007/s00018-005-5386-7>
- Mildvan, A.S., Z. Xia, H.F. Azurmendi, V. Saraswat, P.M. Legler, M.A. Masiah, S.B. Gabelli, M.A. Bianchet, L.W. Kang, and L.M. Amzel. 2005. Structures and mechanisms of Nudix hydrolases. *Arch. Biochem. Biophys.* 433:129–143. <https://doi.org/10.1016/j.abb.2004.08.017>
- Minkler, P.E., J. Kerner, S.T. Ingalls, and C.L. Hoppel. 2008. Novel isolation procedure for short-, medium-, and long-chain acyl-coenzyme A esters from tissue. *Anal. Biochem.* 376:275–276. <https://doi.org/10.1016/j.jab.2008.02.022>
- Miranda, D.A., J.-H. Kim, L.N. Nguyen, W. Cheng, B.C. Tan, V.J. Goh, J.S.Y. Tan, J. Yaligar, B.P. Kn, S.S. Velan, et al. 2014. Fat storage-inducing transmembrane protein 2 is required for normal fat storage in adipose tissue. *J. Biol. Chem.* 289:9560–9572. <https://doi.org/10.1074/jbc.M114.547687>
- Moir, R.D., D.A. Gross, D.L. Silver, and I.M. Willis. 2012. SCS3 and YFT2 link transcription of phospholipid biosynthetic genes to ER stress and the UPR. *PLoS Genet.* 8. e1002890. <https://doi.org/10.1371/journal.pgen.1002890>
- Naquet, P., E.W. Kerr, S.D. Vickers, and R. Leonardi. 2020. Regulation of coenzyme A levels by degradation: the ‘ins and outs’. *Prog. Lipid Res.* 78. 101028. <https://doi.org/10.1016/j.plipres.2020.101028>
- Oelkers, P., A. Tinkelenberg, N. Erdeniz, D. Cromley, J.T. Billheimer, and S.L. Sturley. 2000. A lecithin cholesterol acyltransferase-like gene mediates diacylglycerol esterification in yeast. *J. Biol. Chem.* 275:15609–15612. <https://doi.org/10.1074/jbc.C000144200>
- Oelkers, P., D. Cromley, M. Padamsee, J.T. Billheimer, and S.L. Sturley. 2002. The DGAI gene determines a second triglyceride synthetic pathway in yeast. *J. Biol. Chem.* 277:8877–8881. <https://doi.org/10.1074/jbc.M111646200>
- Ofman, R., D. Speijer, R. Leen, and R.J.A. Wanders. 2006. Proteomic analysis of mouse kidney peroxisomes: identification of RP2p as a peroxisomal nudix hydrolase with acyl-CoA diphosphatase activity. *Biochem. J.* 393: 537–543. <https://doi.org/10.1042/BJ20050893>
- Piccolis, M., L.M. Bond, M. Kampmann, P. Pulimeno, C. Chitraju, C.B.K. Jayson, L.P. Vaites, S. Boland, Z.W. Lai, K.R. Gabriel, et al. 2019. Probing the global cellular responses to lipotoxicity caused by saturated fatty acids. *Mol. Cell.* 74:32–44.e8. <https://doi.org/10.1016/j.molcel.2019.01.036>
- Roesdink, J.B.T.M., and A. Meijster. 2000. The watershed transform: definitions, algorithms and parallelization strategies. *Fundam. Inform.* 41: 187–228.
- Sanjana, N.E., O. Shalem, and F. Zhang. 2014. Improved vectors and genome-wide libraries for CRISPR screening. *Nat. Methods*. 11:783–784. <https://doi.org/10.1038/nmeth.3047>
- Santinho, A., V.T. Salo, A. Chorlay, S. Li, X. Zhou, M. Omrane, E. Ikonen, and A.R. Thiam. 2020. Membrane curvature catalyzes lipid droplet assembly. *Curr. Biol.* 30:2481–2494.e6. <https://doi.org/10.1016/j.cub.2020.04.066>
- Schuck, S., W.A. Prinz, K.S. Thorn, C. Voss, and P. Walter. 2009. Membrane expansion alleviates endoplasmic reticulum stress independently of the unfolded protein response. *J. Cell Biol.* 187:525–536. <https://doi.org/10.1083/jcb.200907074>
- Shimabukuro, M., Y.-T. Zhou, M. Levi, and R.H. Unger. 1998. Fatty acid-induced beta cell apoptosis: a link between obesity and diabetes. *Proc. Natl. Acad. Sci. USA*. 95:2498–2502.
- Sigal, Y.J., M.I. McDermott, and A.J. Morris. 2005. Integral membrane lipid phosphatases/phosphotransferases: common structure and diverse functions. *Biochem. J.* 387:281–293. <https://doi.org/10.1042/BJ20041771>
- Sorger, D., and G. Daum. 2002. Synthesis of triacylglycerols by the acyl-coenzyme A:diacyl-glycerol acyltransferase Dgalp in lipid particles of the yeast *Saccharomyces cerevisiae*. *J. Bacteriol.* 184:519–524. <https://doi.org/10.1128/JB.184.2.519-524.2002>
- Soupe, E., and F.A. Kuypers. 2008. Mammalian long-chain acyl-CoA synthetases. *Exp. Biol. Med. (Maywood)*. 233:507–521. <https://doi.org/10.3181/0710-MR-287>
- Surma, M.A., C. Klose, D. Peng, M. Shales, C. Mrejen, A. Stefanko, H. Braberg, D.E. Gordon, D. Vorkel, C.S. Ejsing, et al. 2013. A lipid E-MAP identifies Ubx2 as a critical regulator of lipid saturation and lipid bilayer stress. *Mol. Cell.* 51:519–530. <https://doi.org/10.1016/j.molcel.2013.06.014>
- Testerink, N., M.H.M. van der Sanden, M. Houweling, J.B. Helms, and A.B. Vaandrager. 2009. Depletion of phosphatidylcholine affects endoplasmic reticulum morphology and protein traffic at the Golgi complex. *J. Lipid Res.* 50:2182–2192. <https://doi.org/10.1194/jlr.M800660-JLR200>
- Unger, R.H., and Y.-T. Zhou. 2001. Lipotoxicity of beta-cells in obesity and in other causes of fatty acid spillover. *Diabetes*. 50(Suppl 1):S118–S121. <https://doi.org/10.2337/diabetes.50.2007.S118>
- Villa-García, M.J., M.S. Choi, F.I. Hinz, M.L. Gaspar, S.A. Jesch, and S.A. Henry. 2011. Genome-wide screen for inositol auxotrophy in *Saccharomyces cerevisiae* implicates lipid metabolism in stress response signaling. *Mol. Genet. Genomics*. 285:125–149. <https://doi.org/10.1007/s00438-010-0592-x>
- Voeltz, Gia K, William A Prinz, Yoko Shibata, Julia M Rist, and Tom A Rapoport. 2006. A class of membrane proteins shaping the tubular endoplasmic reticulum. *Cell*. 124(3):573–586. <https://doi.org/10.1016/j.cell.2005.11.047>
- Volmer, R., and D. Ron. 2015. Lipid-dependent regulation of the unfolded protein response. *Curr. Opin. Cell Biol.* 33:67–73. <https://doi.org/10.1016/j.ceb.2014.12.002>
- Walther, T.C., J. Chung, and R.V. Farese, Jr. 2017. Lipid droplet biogenesis. *Annu. Rev. Cell Dev. Biol.* 33:491–510. <https://doi.org/10.1146/annurev-cellbio-100616-060608>
- Wang, H., M. Becuwe, B.E. Housden, C. Chitraju, A.J. Porras, M.M. Graham, X.N. Liu, A.R. Thiam, D.B. Savage, A.K. Agarwal, et al. 2016. Seipin is required for converting nascent to mature lipid droplets. *eLife*. 5. e16582. <https://doi.org/10.7554/eLife.16582>
- Yen, C.L.E., S.J. Stone, S. Koliwad, C. Harris, and R.V. Farese, Jr. 2008. Thematic review series: glycerolipids. DGAT enzymes and triacylglycerol biosynthesis. *J. Lipid Res.* 49:2283–2301. <https://doi.org/10.1194/jlr.R800018-JLR200>
- Zazo Seco, C., A. Castells-Nobau, S.-H. Joo, M. Schraders, J.N. Foo, M. van der Voet, S.S. Velan, B. Nijhof, J. Oostrik, E. de Vriese, et al. 2017. A homozygous *FITM2* mutation causes a deafness-dystonia syndrome with motor regression and signs of ichthyosis and sensory neuropathy. *Dis. Model. Mech.* 10:105–118. <https://doi.org/10.1242/dmm.026476>

Supplemental material

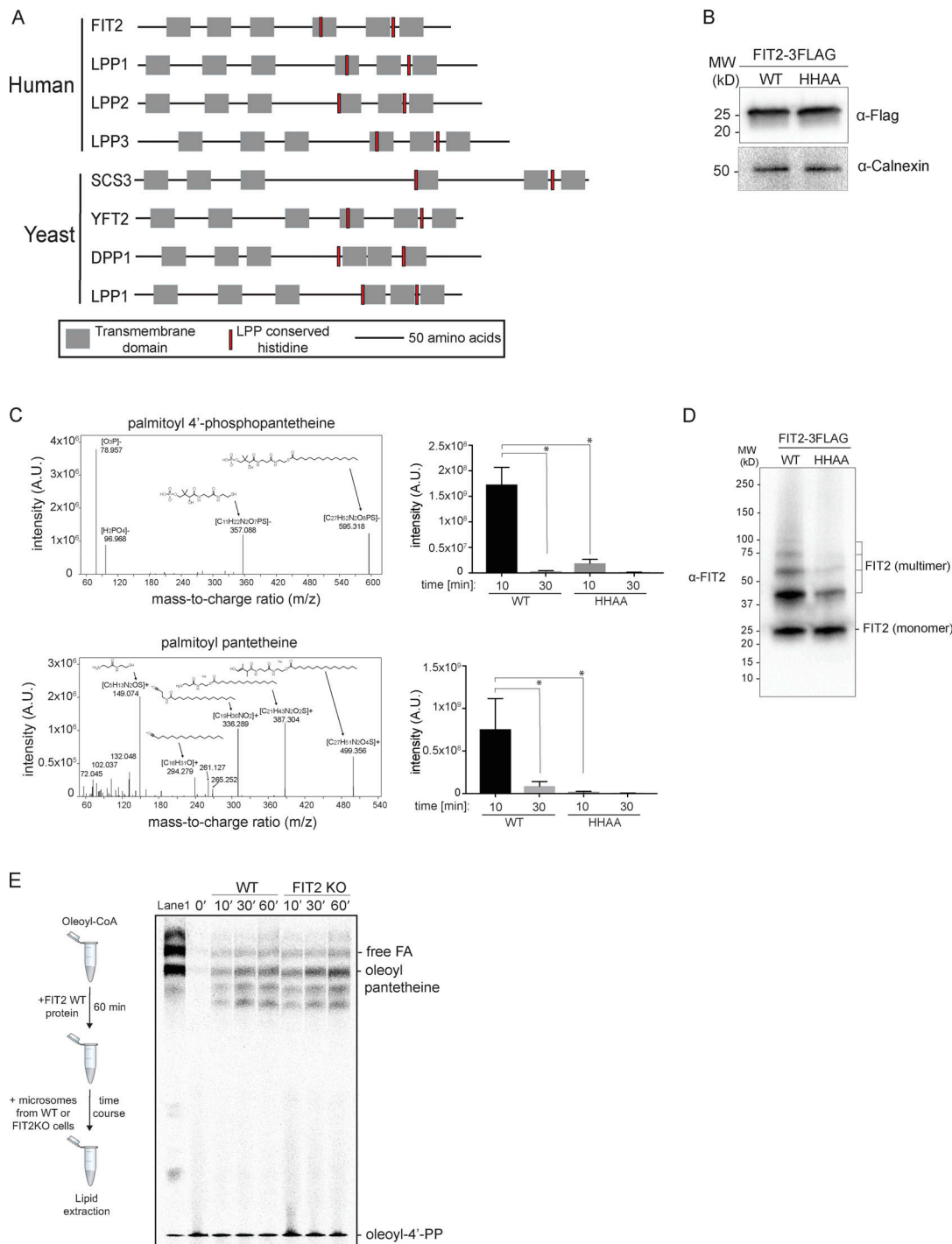


Figure S1. FIT2 homology with LPP enzymes and characterization of FIT2 activity. **(A)** FIT2 and its yeast homologue Scs3 share homology with LPP enzymes. FIT2 overall topology (six transmembrane domains) and the positions of C2 and C3 histidines are similar to those of other LPP enzymes (Lpp1, Lpp2, and Lpp3). Also shown are Scs3, its homologue Yft2, and some yeast LPP members (Dpp1 and Lpp1). **(B)** Western blotting of protein extracts from microsomal fractions purified from GnT1⁻ 293 cells overexpressing FIT2 WT or FIT2 HHAA. **(C)** MS analysis of FIT2 products using palmitoyl-CoA as a substrate. Identification of lipids 1 and 2 by MS in microsomal extracts overexpressing either FIT2 WT or FIT2 HHAA loaded with palmitoyl-CoA. MS2 fragmentation patterns of ions 595.318 D and 499.356 D corresponding to palmitoyl 4'-phosphopantetheine (upper panel) and palmitoyl pantetheine (lower panel), respectively, as well as the structures assigned for each main peak, are presented. Bar graphs showing intensity level of these metabolites found in microsomes overexpressing FIT2 WT or FIT2 HHAA at 10 and 30 min after palmitoyl-CoA loading are presented (mean values ± SD; two-way ANOVA with Sidak test; *, P < 0.0001). **(D)** Western blot of purified FIT2 WT and HHAA proteins produced from GnT1⁻ 293 cells. **(E)** Oleoyl pantetheine is produced by an enzyme independent of FIT2. Schematic representation of the experiment is shown at left. Recombinant FIT2 WT was incubated for 60 min with mixed unlabeled and radiolabeled [¹⁴C] oleoyl-CoA, and then microsomes purified from FIT2 WT or FIT2-KO SUM159 cells were added and incubated for the indicated time. As a control to visualize oleoyl pantetheine in lane 1, purified microsomes from human GnT1⁻ 293 cells overexpressing FIT2 WT were incubated with 25 μM mixed unlabeled and radiolabeled [¹⁴C]oleoyl-CoA for 10 min. Lipids were separated by TLC with polar lipid solvent. Oleoyl-4'-PP: oleoyl 4'-phosphopantetheine.

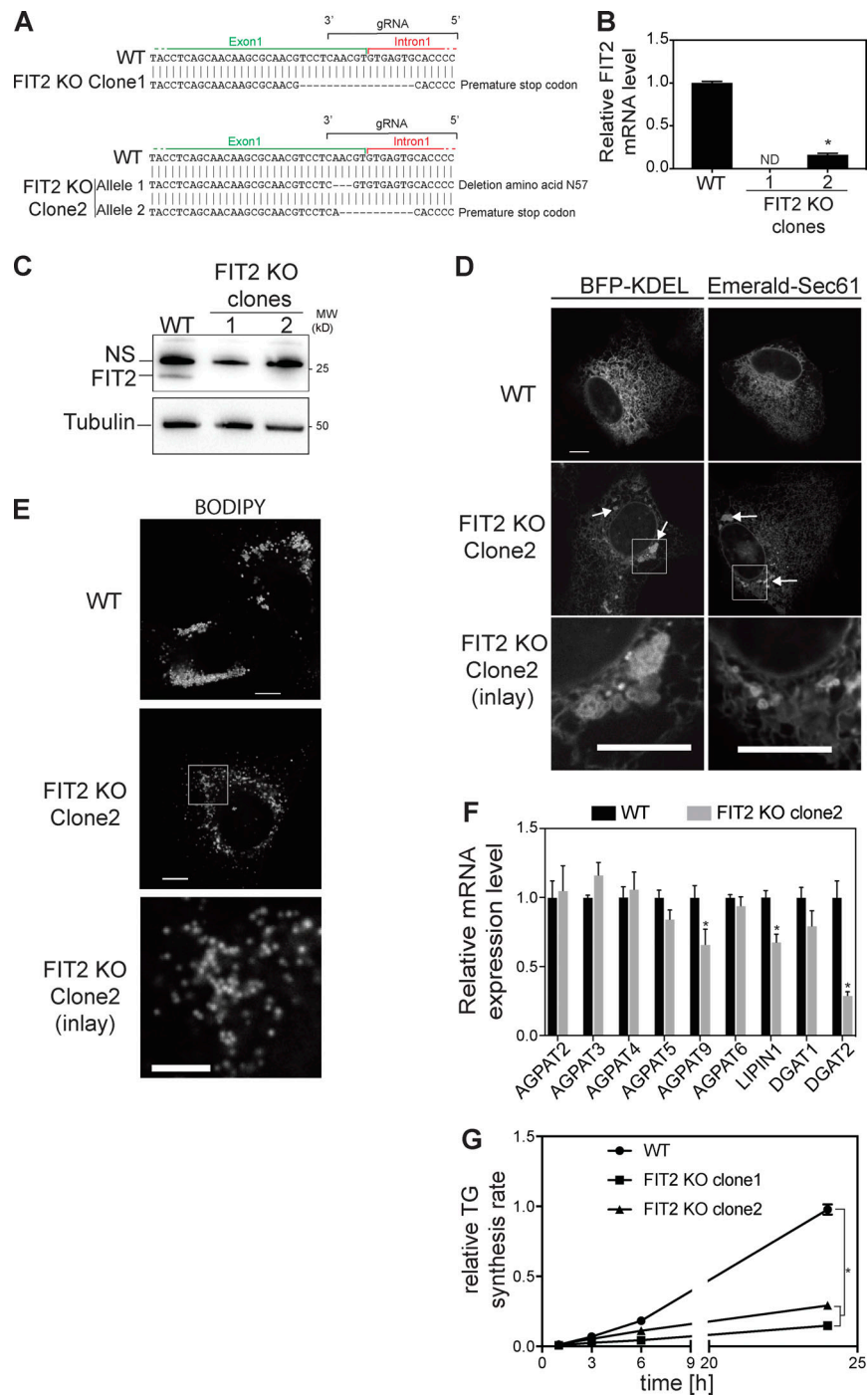


Figure S2. **Characterization of FIT2-KO SUM159 clones.** (A) Sequence of genome-edited region in FIT2-KO clones 1 and 2. In FIT2-KO clone 1, a 17-bp deletion at the end of exon 1 in the FIT2 locus yields a frame shift. In FIT2-KO clone 2, an 11-bp deletion at the end of exon 1 in FIT2 locus yields a frame shift. In the other allele, a 3-bp deletion leads to deletion of an asparagine at position 57. The gRNA position in the WT genome is indicated. (B) FIT2 mRNA levels in FIT2 WT and FIT2-KO clones as determined by qPCR. Values represent mean \pm SD relative to WT cells; $n = 3$ (two-way ANOVA with Sidak test; *, $P < 0.001$). (C) No detectable FIT2 protein was observed for either FIT2-KO clone. Western blot of FIT2 WT, FIT2-KO clone 1, and FIT2-KO clone 2 crude extracts examined with anti-FIT2 antibody. (D) ER morphology was affected in FIT2-KO clone 2. Confocal images of FIT2 WT and FIT2-KO clone 2 cells transiently expressing the ER marker ssBFP-KDEL or GFP-Sec61 β . White arrows indicate ER aberrations. Scale bar = 10 μ m. (E) FIT2-KO clone 2 cells form fewer and smaller LDs. Confocal images of FIT2 WT and FIT2-KO clone 2 cells treated with 500 μ M oleic acid for 48 h. LDs were stained with BODIPY. Representative confocal images are presented. Scale bar = 10 μ m. (F) FIT2-KO clone 2 displayed an alteration of lipid synthesis enzyme expression. mRNA levels of genes involved in the Kennedy pathway were assessed by qPCR analysis of FIT2 WT and FIT2-KO clone 2 cells. Values represent mean \pm SD relative to WT cell level; $n = 3$ (two-way ANOVA with Sidak test; *, $P < 0.05$). (G) FIT2-KO clone 2 displayed a defect in TG synthesis. FIT2 WT and FIT2-KO clone 2 cells were pulse labeled with [14 C]oleic acid, and incorporation into TG was measured over time by TLC. Mean value of TG band intensity was plotted over time and quantified from three independent measurements. Values were calculated relative to the value of WT cells at 24 h (two-way ANOVA with Sidak test; *, $P < 0.01$). The TG synthesis rate of FIT2-KO clone 1 is also shown for comparison.

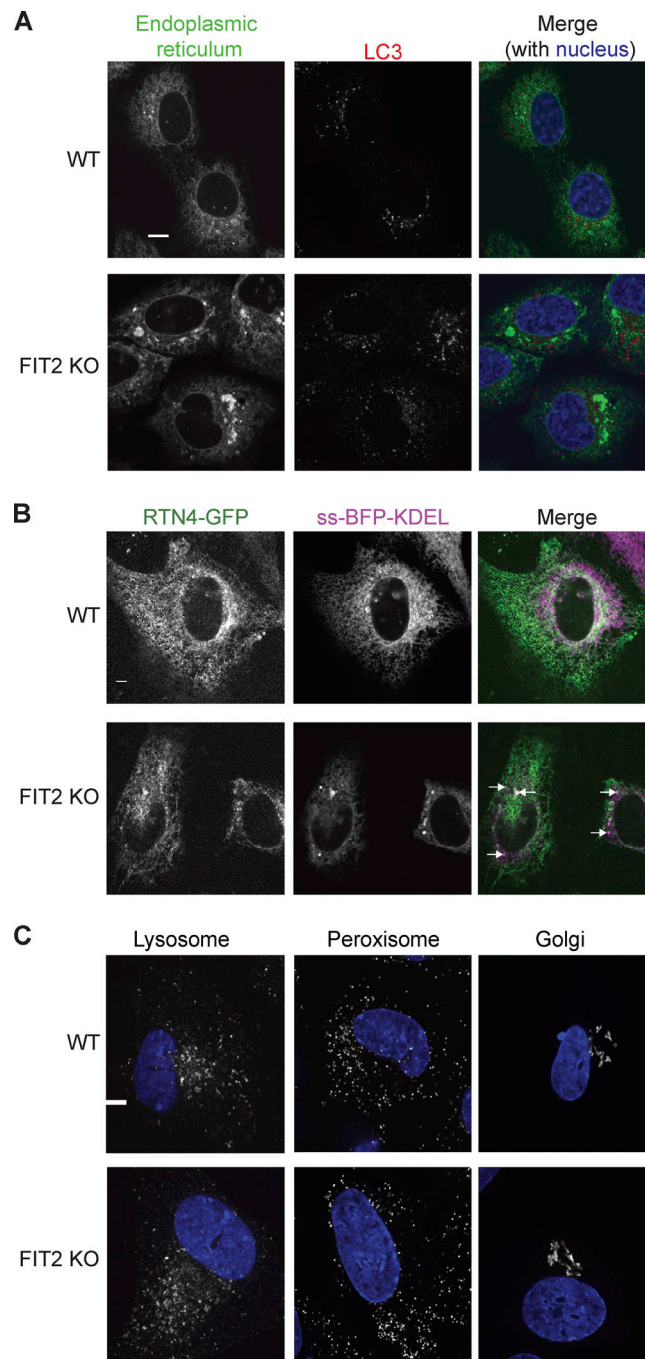


Figure S3. **Impact of FIT2 deletion on other organelles.** **(A)** Representative confocal images of immunofluorescence using antibodies targeting markers of the ER (anti-protein disulfide isomerase) and autophagy (anti-LC3). Scale bar = 10 μ m. **(B)** Representative confocal images of FIT2 WT and FIT2-KO cells cotransfected with RTN4a-GFP and ssBFP-KDEL. White arrows indicate the presence of ER whorls. Scale bar = 5 μ m. **(C)** Representative confocal images of immunofluorescence using antibodies targeting markers of the Golgi apparatus (anti-GM130), peroxisome (anti-catalase), and lysosome (anti-LAMP1) in FIT2 WT and FIT2-KO SUM159 cells. Scale bar = 10 μ m.

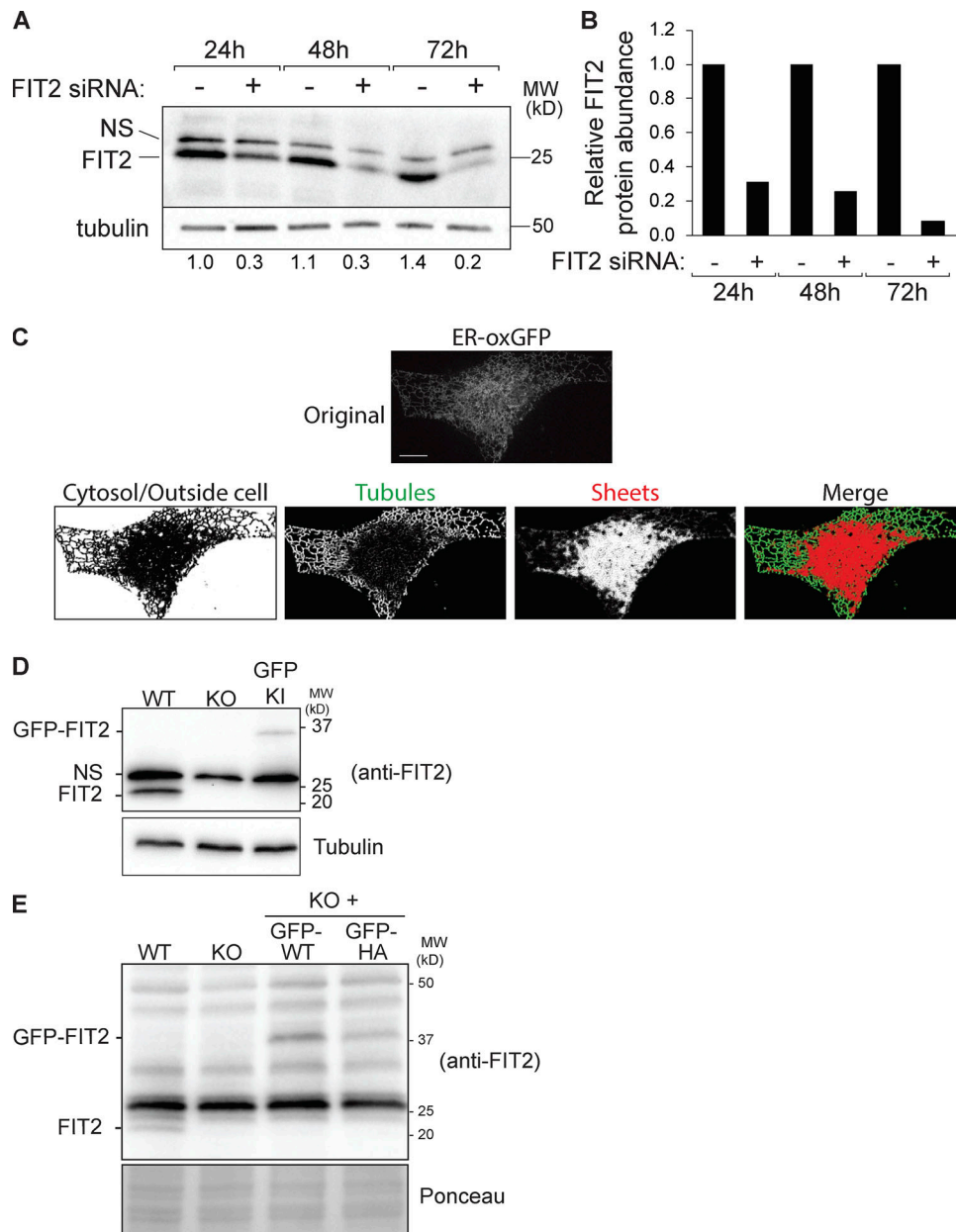


Figure S4. **FIT2-KD efficiency, ER feature quantification, and characterization of the cell line expressing endogenously GFP-tagged FIT2.** (A) Cells treated with FIT2 siRNA for 72 h reduced FIT2 protein levels by 80%. Cells were treated with control or FIT2 siRNA for the indicated time, and FIT2-KD efficiency was determined by Western blotting with an anti-FIT2 antibody. Tubulin was used as a loading control. Quantification of band intensities relative to control siRNA at 24 h is shown under the tubulin panel. (B) FIT2 protein abundance based on Western blots in A was plotted relative to control siRNA for each time point. (C) Segmentation of ER features by machine learning. Cells treated with control siRNA for 72 h transiently expressing the ER marker ER-oxGFP were imaged. One confocal image of a Z-stack is presented (original image). As detailed in the Materials and methods section, machine learning was used to segment the ER features (sheets, tubules, and outside of the cell/cytosol). Scale bar = 10 μ m. (D) Western blot analysis of the CRISPR-engineered GFP knock-in cell line using anti-FIT2 antibody. FIT2 WT and FIT2-KO cell extracts are used as controls. (E) Western blot using anti-FIT2 antibody on crude extracts from WT cells, FIT2-KO cells, and FIT2-KO cells expressing GFP-FIT2 WT or H214A under PGK promoter stably integrated in the safe harbor AAVS1 genomic locus. Endogenous FIT2 was observed at the expected size (22 kD) only in the WT cell extract. GFP-tagged forms of FIT2 were observed at the expected size (45 kD) in WT GFP-FIT2 and H1214A stable cell lines. Ponceau staining was used to control for protein loading.

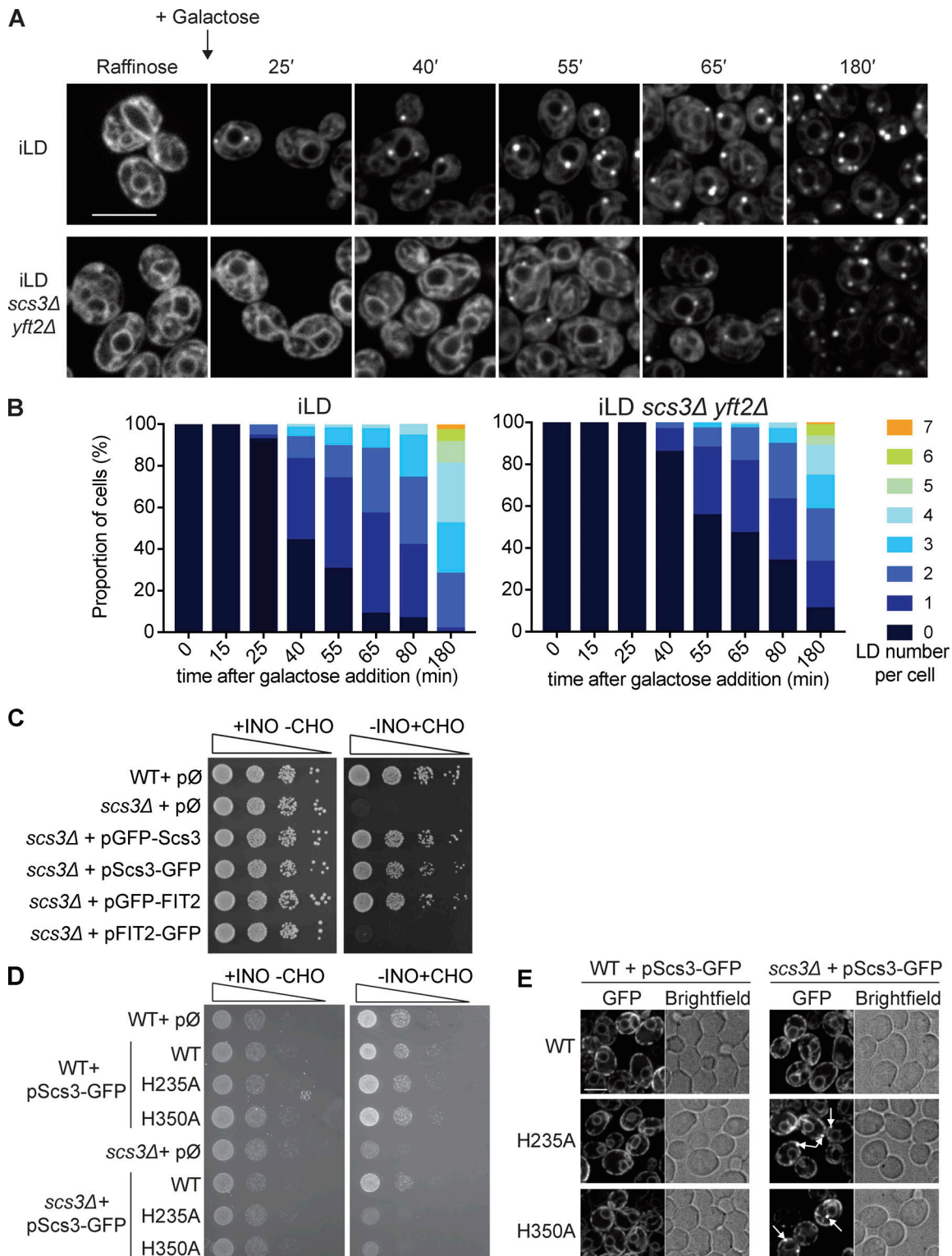


Figure S5. **Yeast assays of FIT2 and SCS3 function.** (A) Representative confocal images of inducible lipid droplet (iLD) strain deleted for *SCS3* and *YFT2* (iLD *scs3Δ yft2Δ*) or not (iLD) after overnight growth in raffinose (repressed LD condition) and after galactose addition (induced LD condition) at the indicated times. LDs were stained with BODIPY 493/503. Scale bar = 5 μ m. (B) Cells were classified depending on their number of LDs over time (from 0 to 7 LDs per cell). Results are presented as a percentage of cells for each time point after galactose addition ($n = 100$ to 150 cells). (C) N- and C-terminally GFP-tagged Scs3 orthologues are functional, but only N-terminally GFP-tagged FIT2 is functional. N- and C-terminally GFP-tagged versions of Scs3 and FIT2 expressed from plasmids in *scs3Δ* cells were grown on complete (+INO-CHO) or inositol-depleted medium (-INO+CHO). (D and E) Scs3 LPP mutants do not have dominant-negative effects. (D) WT or LPP mutant forms of Scs3 expressed from plasmid in WT cells were grown on complete (+INO-CHO) or inositol-depleted medium (-INO+CHO) for 2 d, and (E) their subcellular localizations were assessed by confocal fluorescence microscopy. Localization of the same constructs in *scs3Δ* cells is also presented. ER whorls are indicated by white arrows. Scale bar = 5 μ m.

Provided online are three tables. Table S1 lists qPCR primers, Table S2 lists plasmids, and Table S3 lists yeast strains used in this study.